

Depth-dependence of seismic velocity change associated with the 2011 Tohoku earthquake, Japan, revealed from repeating earthquake analysis and finite-difference wave propagation simulation

Kaoru Sawazaki,^{1,2} Hisanori Kimura,¹ Katsuhiko Shiomi,¹ Naoki Uchida,³ Ryota Takagi^{3,4} and Roel Snieder²

¹National Research Institute for Earth Science and Disaster Prevention, 3-1, Tennodai, Tsukuba, Ibaraki 305-0006, Japan. E-mail: sawa@bosai.go.jp

²Center for Wave Phenomena, Department of Geophysics, Colorado School of Mines, 924 16th Street, Golden, CO 80401, USA

³Graduate School of Science, Tohoku University, 6-3, Aramaki Aza-Aoba, Aoba-ku, Sendai 980-8578, Japan

⁴Earthquake Research Institute, University of Tokyo, Tokyo, Japan

Accepted 2015 January 7. Received 2015 January 6; in original form 2014 July 6

SUMMARY

We detect time-lapse changes in seismic velocity associated with the 2011 Tohoku earthquake, Japan (M_w 9.0), by applying the moving time window cross-correlation analysis to repeating earthquake records registered by Hi-net borehole seismograms. The phase delay curve of the repeating earthquake records demonstrates up to 0.2 per cent apparent velocity reduction for S -wave time windows, while the reduction is only 0.1 per cent at the maximum for P -wave time windows. The apparent velocity reductions for S -wave time windows are especially large for offshore region near the large slip area of the Tohoku earthquake. To investigate the sensitivity of the phase delay curve to partial velocity change, we perform a finite difference (FD) wave propagation simulation using short-wavelength random inhomogeneous media. We found that a 1 per cent velocity reduction at the top 150 m depth (shallow zone) is the most possible model to explain the observed phase delay curve. The evaluated velocity reduction at the shallow zone is consistent with previous studies that detected velocity changes due to strong ground motion. Through the FD simulation, we also found that displacement of the source location after the Tohoku earthquake is not likely the primary cause of the observed apparent velocity change. The average velocity reduction at depths from 150 m to 80 km (deep zone) is evaluated to be much smaller than 0.1 per cent. This small velocity reduction at the deep zone can be caused by a static strain change due to the Tohoku earthquake and its post-seismic deformation.

Key words: Time-series analysis; Interferometry; Body waves; Wave scattering and diffraction; Wave propagation.

1 INTRODUCTION

The 2011 Tohoku earthquake, Japan (M_w 9.0), was the fourth largest earthquake since modern seismograph network has been installed. By using near-field and far-field seismic records (e.g. Suzuki *et al.* 2011; Yoshida *et al.* 2011), terrestrial GPS and seafloor GPS/Acoustic displacement data (e.g. Iinuma *et al.* 2012), bathymetry changes (e.g. Fujiwara *et al.* 2011; Kodaira *et al.* 2012), and Tsunami waveform data (e.g. Satake *et al.* 2013), researchers have detected a large slip up to 85 m near the Japan trench. Strong accelerations up to 3000 Gal were widely recorded in northeastern Japan (e.g. Furumura *et al.* 2011). A tremendous number of aftershocks, induced seismicity, and a post-seismic slip with a cumulative M_w of 8.5 followed the main shock (e.g. Ozawa *et al.* 2012). Medium parameters such as seismic wave velocities, anisotropy,

intrinsic attenuation and scattering coefficient widely changed as a consequence of the Tohoku earthquake.

Correlation functions of ambient noise record have been used to detect the medium changes at depths up to several kilometres (e.g. Wegler & Sens-Schönfelder 2007). Using the autocorrelation function (ACF) of ambient noise records registered by Hi-net [High Sensitivity Seismograph Network Japan, operated by National Research Institute for Earth Science and Disaster Prevention (NIED)], Minato *et al.* (2012) detected up to 1.5 per cent velocity reduction in northeastern Japan after the Tohoku earthquake. Brenguier *et al.* (2014) used cross-correlation function (CCF) of ambient noise records of Hi-net and found much smaller velocity reductions, less than 0.05 per cent. Applying a sensitivity analysis to CCF of ambient noise records before and after the 2008 Iwate-Miyagi Nairiku earthquake, Japan (M_w 6.9), Takagi *et al.* (2012)

reported a localized velocity reduction at the subsurface shallower than a few hundred metres' depth. Applying the CCF technique to the same earthquake using different frequency bands, Hobiger *et al.* (2012) retrieved the greater velocity reductions at the higher frequencies, which indicates that the velocity change is localized near the shallow subsurface. However, we must recognize that the distribution of noise source can cause misdetection in velocity change if it temporarily varies significantly during the analysed time period.

Analysis of repeatable source is another technique that can reveal depth dependence of velocity change. The moving time window cross-correlation analysis (MTWCA) developed by Poupinet *et al.* (1984) has been widely applied to records of artificial repeatable sources and multiplets of natural earthquakes (e.g. Nishimura *et al.* 2005; Chen *et al.* 2008; Yu *et al.* 2013). The theoretical background of the MTWCA is summarized later as the Coda Wave Interferometry by Snieder *et al.* (2002). Applying the MTWCA to seismograms recorded on the ground surface and at the borehole bottom, Rubinstein & Beroza (2005) reported that the velocity change after the 2004 Parkfield earthquake, USA (M_w 6.0), is concentrated near the ground surface. Several researchers have reported a strong correlation between intensity of ground motion and amount of velocity reduction ratio, which implies that strong ground motion, and subsequent damage in the shallow ground, is the primary cause of the seismic velocity reduction (e.g. Peng & Ben-Zion 2006; Rubinstein *et al.* 2007; Takagi & Okada 2012).

Nevertheless, there are also reports that demonstrate velocity changes at the deeper zones which are not exposed to strong ground motion. Maeda *et al.* (2010) detected a velocity reduction associated with the earthquake swarm (the maximum M_L is 5.0) at Kyushu Island, Japan, through the ACF analysis of Hi-net ambient noise record. Analysing the lapse-time dependence of the ACF phase delay curve, they concluded that the velocity change is localized at 15 km depth; beneath the swarm zone. Brenguier *et al.* (2008) and Rivet *et al.* (2011) reported velocity reductions associated with the post-seismic relaxation at Parkfield, USA, and with the slow slip at the Guerrero region, Mexico, respectively, where strong motion is not considered to be the primary cause of the medium changes. Rubinstein *et al.* (2007) applied the MTWCA to repeating earthquake records and suggested that the rupture zone of the 2003 Tokachi-Oki earthquake, Japan (M_w 8.2), or the shallow crust above it represents the region where seismic velocities are reduced after the main shock. Wegler *et al.* (2009) detected almost the same velocity reductions using frequency ranges of 0.1–0.5 and 2–8 Hz for the 2004 mid-Niigata earthquake, Japan (M_w 6.7), and concluded that the velocity change is not restricted to the shallow subsurface. Thus, velocity changes have been observed not only at the shallow subsurface but also at the deeper zone.

Examining the dominant wave type of used seismograms (body wave or surface wave) and depth sensitivity of each wave type is important to constrain depth dependence of velocity change. Obermann *et al.* (2013) performed a 2-D finite difference (FD) wave propagation simulation using a random inhomogeneous medium and a constant background velocity, where the source is located on the free surface. They revealed that energy of backscattered body waves gradually becomes dominant as the lapse time increases. Consequently, the later coda of ambient noise CCF is more sensitive to velocity change in the deeper subsurface compared to the earlier part. In the real Earth, however, both background velocity and medium heterogeneity vary with depth, and the energy balance of body and surface waves could be different from the situation that Obermann *et al.* (2013) examined. Also, repeating natural sources

are usually located at a depth of kilometres, not on the ground surface. Performing an FD simulation using more realistic source and medium model is necessary if we want to interpret the result of seismic interferometry obtained from seismograms of natural repeating earthquakes.

The purpose of this study is to provide a rough sketch of the spatial variation of velocity changes associated with the Tohoku earthquake through observation and numerical modelling. We measure phase delay curve by applying the MTWCA to two seismograms of repeating earthquakes, which are recorded before and after the Tohoku earthquake, respectively. To examine the sensitivity of the observed phase delay curve to partial velocity change, we perform a 2-D FD wave propagation simulation using a 1-D background velocity structure and random inhomogeneous media. The velocity change evaluated at the depths from 0 to 150 m is compared to known velocity changes revealed from deconvolution analysis of borehole seismograms (Sawazaki & Snieder 2013). The velocity change evaluated at the depths from 150 m to 80 km is compared to theoretical velocity change computed from the finite deformation theory and geodetic data obtained before and after the Tohoku earthquake. We also examine how the displacement of source location of the repeating cluster affects the observed phase delay curve.

2 DATA

Fig. 1 shows locations of Hi-net stations (triangles) and epicentres of repeating earthquake clusters (circles) used in this study. Each Hi-net station is equipped with a three component velocity seismometer, which is installed at the bottom of a borehole with the depth ranging from 100 to 3500 m. The electric signal is digitized at 100 Hz sampling frequency with a dynamic range of $\pm 2.5 \text{ cm s}^{-1}$ and 27 bit resolution. Frequency response of the recording system is almost flat from 2 to 30 Hz. Since each Hi-net sensor is collocated with a borehole acceleration seismometer of KiK-net (the Strong-motion Seismograph Network in Japan operated by NIED), medium changes detected by the Hi-net records are directly comparable to that detected by the KiK-net records (Sawazaki & Snieder 2013). Details of the Hi-net acquisition system are summarized by Obara *et al.* (2005).

We analyse 218 clusters of repeating earthquakes on and around the faulting area of the Tohoku earthquake and obtain 3980 cluster–station pairs in total (see grey lines in Fig. 1). Each cluster–station pair includes at least one earthquake record in each period from 2003 March 1 to 2011 March 11 (before the Tohoku earthquake) and from 2011 March 11 to 2012 March 10 (after the Tohoku earthquake). We use the seismogram pairs whose average coherence from the P -wave onset time to 38.4 s later at 1–10 Hz is larger than 0.8 for all three components. Hypocentral distance and hypocentral depth range from 35 to 286 km and from 4 to 85 km, respectively. Because mostly inland stations are used to determine the hypocentre, locations of offshore events are poorly constrained. Magnitude of repeating earthquakes distributes from 2.5 to 5.1, and the variation of magnitude in a same cluster after the Tohoku earthquake is 0.4 at the maximum. This change of magnitude is caused by acceleration of loading rate around the clusters due to post-seismic deformation after the Tohoku earthquake (Uchida *et al.* 2015).

As shown in Fig. 1, the activity of repeating earthquake has been low on the large slip area (over 10 m slip) after the Tohoku earthquake. This quiescence of seismicity is interpreted as a consequence of almost complete stress release by the main shock

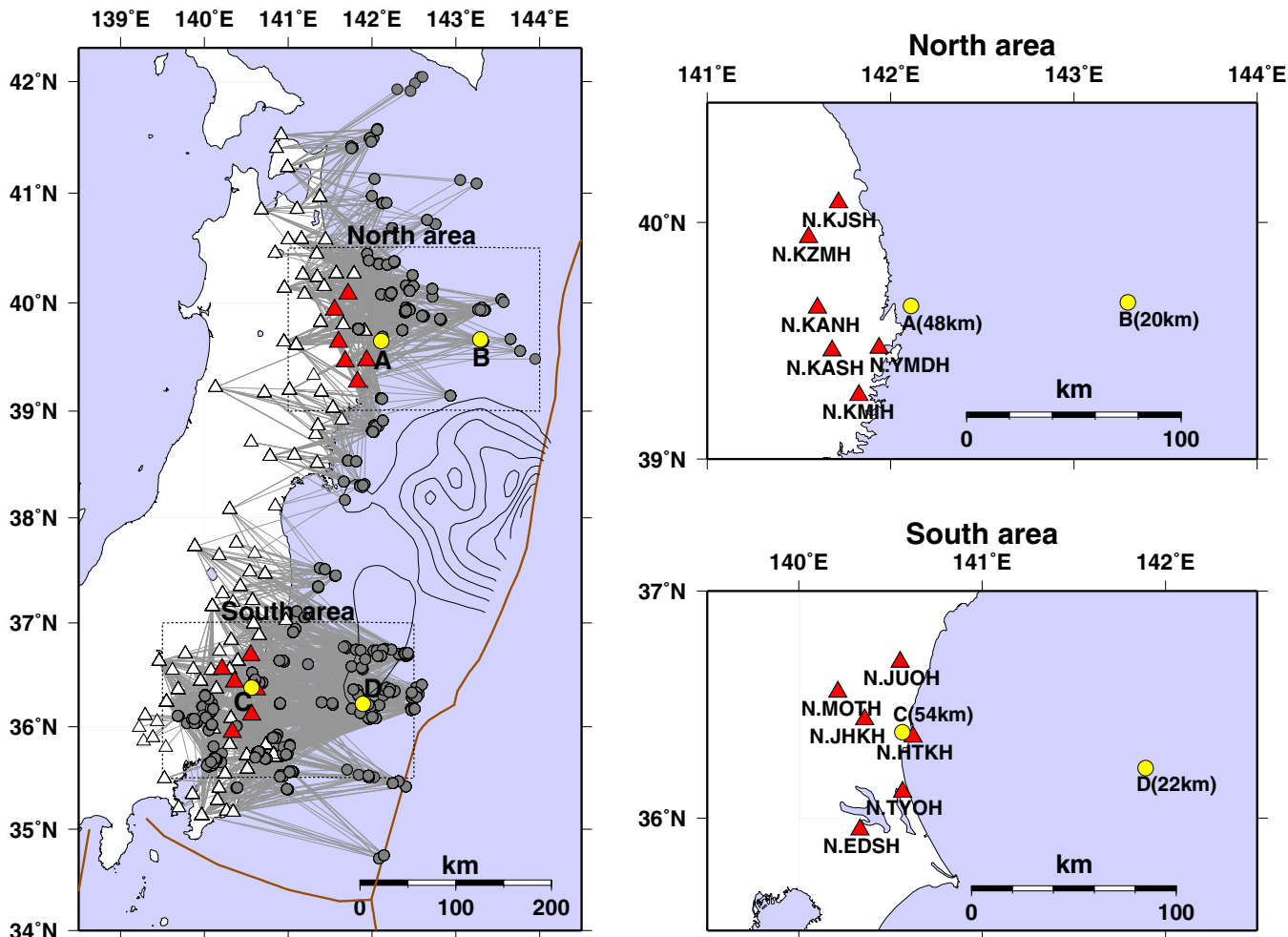


Figure 1. Map of Hi-net stations (triangles) and clusters of repeating earthquakes (circles) used in this study. The grey lines connect the cluster–station pairs used in MTWCA. The black contour curves represent slip distribution of the Tohoku earthquake by 10 m slip interval following Iinuma *et al.* (2012). The clusters A, B, C, D (yellow circles) and the stations drawn by red triangles are used to show phase delay curves in Fig. 3. The brown curves represent plate boundaries. The areas framed by dotted rectangles (north and south areas) are magnified on the right of the map. The brackets in the magnified figures denote hypocentral depth of the clusters.

rupturing (Uchida & Matsuzawa 2013). We therefore, cannot use repeating clusters located on this large slip area.

3 ANALYSIS PROCEDURE

Firstly we deconvolve response function of the Hi-net recording system following Maeda *et al.* (2011), and correct for horizontal polarization error of each Hi-net sensor following Shiomi *et al.* (2003). Then we rotate two horizontal seismograms to transverse and radial components and apply a 1–10 Hz bandpass filter to each component.

Fig. 2(a) shows the radial component seismograms of repeating earthquakes in cluster B recorded at station N.KASH. The black and red curves represent seismograms recorded on 2003 April 3 and 2011 June 11, respectively, where the Tohoku earthquake occurred on 2011 March 11 between the two dates. The apparent similarity of the two records decreases as the lapse time increases.

We adjust P -wave onset time to zero seconds and set $T = 2.56$ s length time windows every 1.28 s interval after the P -wave onset time. For each time window, a cross coherence function $C_{nb,na}$ is computed using seismograms obtained before (u_{nb}) and after (v_{na})

the main shock in frequency domain as

$$C_{nb,na}(t, \tau) = IFT \left[\frac{\langle u_{nb}(t, f) v_{na}(t, f) \rangle}{\sqrt{|u_{nb}(t, f)|^2 |v_{na}(t, f)|^2}} \right], \quad (1)$$

where t , τ and f are lapse time after the P -wave onset time, lag time of the cross coherence function, and frequency, respectively. The IFT and the bracket in eq. (1) represent taking inverse Fourier transform and applying a Hanning window once for smoothing, respectively. The subscripts nb and na are order number of repeating earthquake occurring before and after the main shock in each cluster, respectively. Hereafter, we omit these subscripts unless they are necessary for description.

By fitting a quadratic function $C'(t, \tau) = a(t)\tau^2 + b(t)\tau + c(t)$ to amplitudes of discrete cross coherence $C(t, \tau_{\max} - \Delta\tau)$, $C(t, \tau_{\max})$ and $C(t, \tau_{\max} + \Delta\tau)$, we obtain phase delay time $\tau_p^{\text{obs}}(t)$ and coherence $\text{coh}(t)$. Here, τ_{\max} and $\Delta\tau$ are the lag-time which gives the maximum coherence amplitude and the time sampling interval (0.01 s for Hi-net system), respectively. Hereafter, we denote the sequence of these three lag-times by $\tau_- \equiv \tau_{\max} - \Delta\tau$, $\tau_0 \equiv \tau_{\max}$ and $\tau_+ \equiv \tau_{\max} + \Delta\tau$. The least-squares solution (Aster *et al.* 2011)

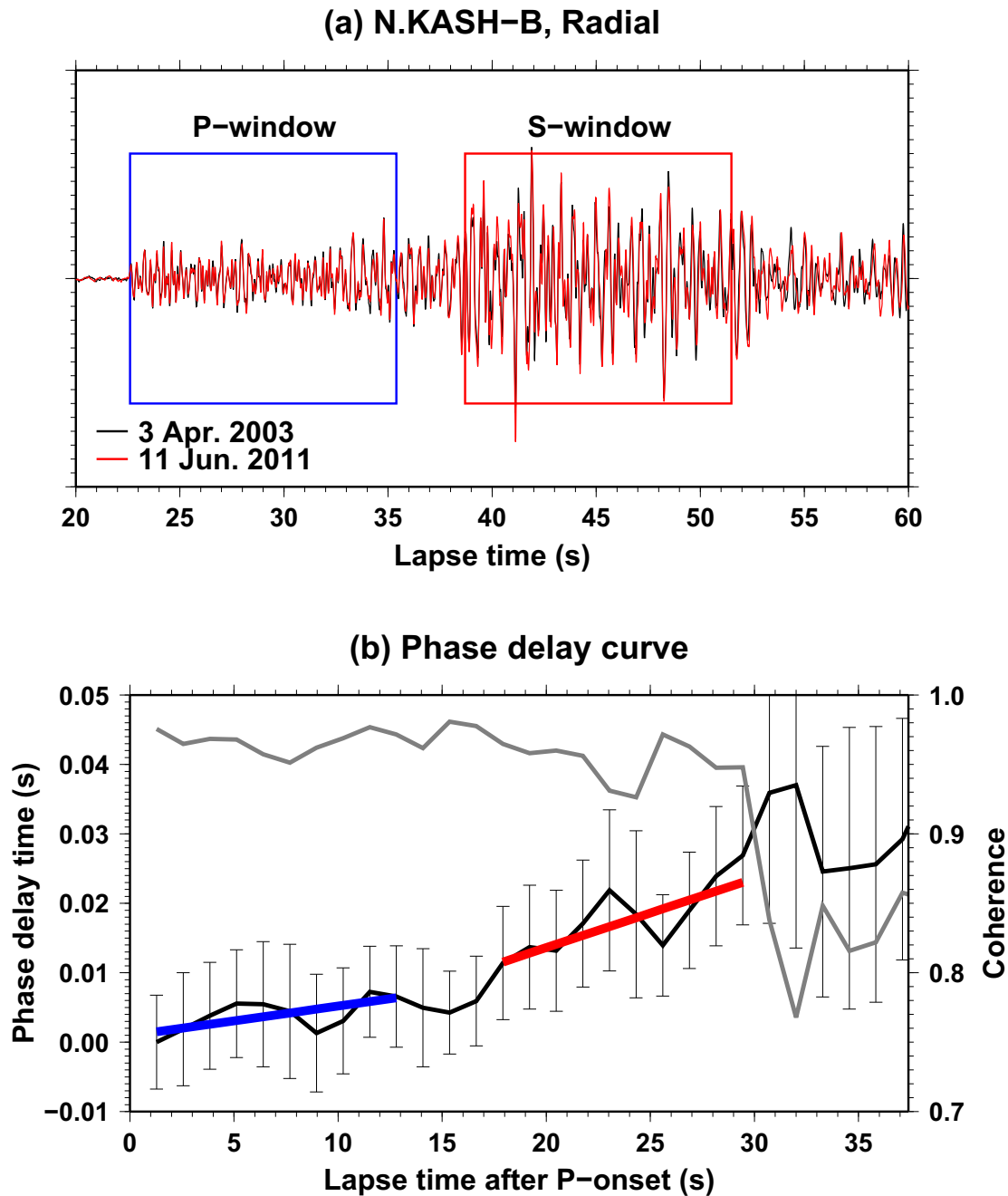


Figure 2. (a) Radial component seismograms of repeating earthquakes in the cluster B recorded at station N.KASH. The black and red seismograms represent events occurring on 2003 April 3 (8 yr before the Tohoku earthquake) and 2011 June 11 (3 months after the Tohoku earthquake), respectively. The blue and red rectangles represent time windows used to calculate apparent velocity change ratios for P and S waves, respectively. (b) Phase delay curve (black curve) and coherence (grey curve) given by eq. (3). The error bar represents 95 per cent confidence interval calculated from eq. (5). The blue and red thick lines represent regression lines of the phase delay curve calculated for P - and S -wave windows, respectively.

for the coefficients of the quadratic function a , b and c is given by

$$\mathbf{M} \equiv \begin{bmatrix} a(t) \\ b(t) \\ c(t) \end{bmatrix} = [\mathbf{G}^T \mathbf{G}]^{-1} \mathbf{G}^T \mathbf{C}$$

$$\mathbf{G} \equiv \begin{bmatrix} \tau_-^2 & \tau_- & 1 \\ \tau_0^2 & \tau_0 & 1 \\ \tau_+^2 & \tau_+ & 1 \end{bmatrix}, \quad \mathbf{C} \equiv \begin{bmatrix} C(t, \tau_-) \\ C(t, \tau_0) \\ C(t, \tau_+) \end{bmatrix}, \quad (2)$$

where \mathbf{M} , \mathbf{G} and \mathbf{C} represent model parameter vector, kernel matrix and data vector, respectively. By solving the least-squares inversion given by eq. (2), we derive τ_p^{obs} and coh as

$$\tau_p^{\text{obs}}(t) = -\frac{b(t)}{2a(t)}$$

$$\text{coh}(t) = c(t) - \frac{b(t)^2}{4a(t)}. \quad (3)$$

Following Ito (1990), we evaluate variance of the phase delay time $\sigma_{\tau_p}^2$ as

$$\sigma_{\tau_p}^2(t) = \frac{I}{8\pi^2 f_L f_H T} \left[\frac{1}{\text{coh}(t)} - 1 \right], \quad (4)$$

where I , f_L and f_H are power of the smoothing window function, and lower and upper cut-off frequencies of the used bandpass filter, respectively. Substituting $I = 0.375T$ for applying a Hanning window once (see Appendix A), $f_L = 1$ Hz, $f_H = 10$ Hz and $T = 2.56$ s to eq. (4), we obtain

$$\sigma_{\tau_p}^2(t) = 0.000475 \times \left[\frac{1}{\text{coh}(t)} - 1 \right] (\text{s}^2). \quad (5)$$

Fig. 2(b) shows phase delay curve (black curve) with its 95 per cent confidence interval (error bar) and coherence (grey curve) computed for the seismograms shown in Fig. 2(a). The phase delay increases as the lapse time increases because scattered wave is more sensitive to change of medium velocity than direct wave (Snieder *et al.* 2002).

The phase delays are observed not only between seismograms obtained before and after the main shock but also among seismograms obtained before the main shock due to occurrence of other large earthquakes, temperature change, precipitation, background plate motion and so on. However, these background velocity changes are smaller than the velocity changes caused by the Tohoku earthquake for most of the used data. Therefore, we compute average ($\tau_{p,na}^{\text{obs}}$) and variance ($\sigma_{\tau_p,na}^2$) of the phase delay curves obtained for the n th earthquake by

$$\tau_{p,na}^{\text{obs}}(t) = \sum_{nb=1}^{Nb} \left[\frac{\tau_{p,na,nb}^{\text{obs}}(t)}{\sigma_{\tau_p,na,nb}^2(t)} \right] / \sum_{nb=1}^{Nb} \left[\frac{1}{\sigma_{\tau_p,na,nb}^2(t)} \right]$$

$$\sigma_{\tau_p,na}^2(t) = 1 / \sum_{nb=1}^{Nb} \left[\frac{1}{\sigma_{\tau_p,na,nb}^2(t)} \right], \quad (6)$$

where Nb is the number of repeating earthquakes recorded before the main shock in each cluster.

Next, we fit a regression line $\tau'(t) = A \cdot t + B$ to the obtained phase delay curve. We set two time windows; one begins from the P -wave onset time (blue rectangle in Fig. 2a), and the other begins from the S -wave onset time (red rectangle in Fig. 2a). Both windows are 12.8 s long length with $N = 10$ discrete phase delay samples. The P -wave window is set only if the P - S traveltime difference is longer than 12.8 s so that the two windows do not overlap. The least-squares solution for the coefficients A and B is given by

$$\mathbf{M} \equiv \begin{pmatrix} A \\ B \end{pmatrix} = [\mathbf{G}^T \text{cov} \mathbf{C}^{-1} \mathbf{G}]^{-1} \mathbf{G}^T \text{cov} \mathbf{C}^{-1} \mathbf{C}$$

$$\text{cov} \mathbf{M} \equiv \begin{pmatrix} \sigma_A^2 & \sigma_{AB}^2 \\ \sigma_{BA}^2 & \sigma_B^2 \end{pmatrix} = 2 [\mathbf{G}^T \text{cov} \mathbf{C}^{-1} \mathbf{G}]^{-1}$$

$$\mathbf{G} \equiv \begin{bmatrix} t_1 \\ \vdots \\ t_N \end{bmatrix} \quad \mathbf{C} \equiv \begin{bmatrix} \tau_p^{\text{obs}}(t_1) \\ \vdots \\ \tau_p^{\text{obs}}(t_N) \end{bmatrix}$$

$$\text{cov} \mathbf{C} \equiv \begin{bmatrix} \sigma_{\tau_p}^2(t_1) & 0 & 0 \\ 0 & \ddots & 0 \\ 0 & 0 & \sigma_{\tau_p}^2(t_N) \end{bmatrix} \quad (7)$$

where $\text{cov} \mathbf{C}$ and $\text{cov} \mathbf{M}$ represent data and model covariance matrix, respectively. The factor of two that multiplies for $\text{cov} \mathbf{M}$ takes into account that the time windows used to calculate each phase delay time half overlap. An example of regression lines for the P - and S -wave windows are shown by blue and red thick lines in Fig. 2(b), respectively. The slope A is converted to apparent velocity change ratio (Snieder *et al.* 2002) using

$$\frac{dV}{V} = -A. \quad (8)$$

4 SPATIO-TEMPORAL VARIATION IN APPARENT VELOCITY CHANGE RATIO

Fig. 3 shows the phase delay curves observed at stations shown by red triangles in Fig. 1 for clusters A, B, C and D. These clusters are located in the north and south areas and their hypocentral depths are 48, 20, 54 and 22 km, respectively. The solid and dotted curves in each panel represent phase delay curves for repeating earthquakes occurring within 3–4 and 8–11 months after the main shock, respectively (occurrence date is written in each panel). The abscissa and ordinate represent lapse time after the P -wave onset time and phase delay time, respectively. The phase delay at the P -wave onset time is adjusted to zero so that the errors in hypocentral time cancel out.

For the near-coast clusters A and C (Figs 3a and c), the phase delay time briefly increases briefly after the S -wave onset time at many stations, while it is fairly constant for the S -coda. The phase delay of the vertical component is generally larger than that of the horizontal components especially for the cluster A in the north area. For the offshore clusters B and D (Figs 3b and d), on the other hand, the slope of the phase delay curve is relatively gentle for direct- P to P -coda, while it becomes steep after the S -wave onset time. Unlike the results for the near-coast clusters, the phase delay continues to increase even for the S -coda for the offshore clusters. The phase delays obtained within 8–11 months after the main shock are slightly smaller than that within 3–4 months after the main shock for most of the cluster–station pairs, which indicates an existence of velocity recovery.

By applying eqs (7) and (8) to the observed phase delay curves, we calculate apparent velocity change ratios. The ratios are averaged for all cluster–station paths that cross 50 km \times 50 km subareas and are mapped in Figs 4(a) (S -wave time window) and b (P -wave time window). The vertical component is used for the mapping. The time period after the main shock is divided into 0–1, 1–3, 3–6 and 6–12 months. The depth dependence of the apparent velocity change ratio is not considered in the mapping because our knowledge on depth sensitivity is limited. Figs 5(a) and (b) are map of the 95 per cent confidence interval of the apparent velocity change ratio for S - and P -wave time windows, respectively.

Up to 0.2 per cent apparent velocity reduction is observed for S -wave time windows at regions surrounding the large slip area. Considering the confidence intervals shown in Fig. 5(a), the observed reduction is significant except for the western part of the large slip area in the period of 0–3 months. The reduction ratio becomes smaller as the distance from the large slip area increases. The apparent velocity continues to recover for 1 yr. On the other hand, the apparent velocity reduction ratio for P -wave time window is mostly less than 0.1 per cent and its recovery is not clearly observed. Such difference in apparent velocity changes for the P - and S -wave time windows is also reported for the 2003 Tokachi-Oki earthquake by Rubinstein *et al.* (2007).

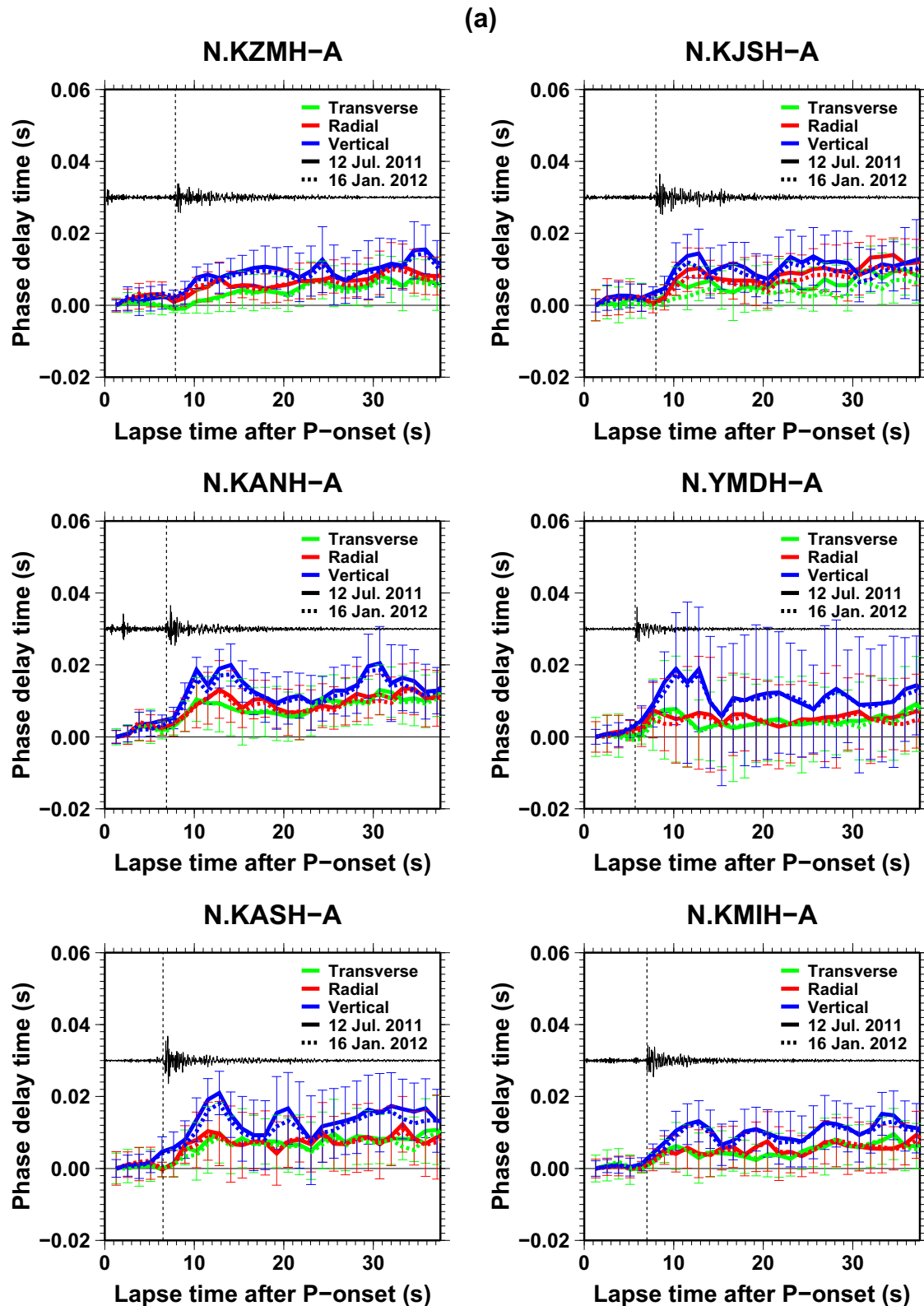


Figure 3. Observed phase delay curves for clusters (a) A, (b) B, (c) C and (d) D at stations drawn by red triangles shown in Fig. 1. The green, red, and blue colours represent the transverse, radial, and vertical components, respectively. The solid and dotted curves are obtained within 3–4 and 8–11 months after the Tohoku earthquake, respectively. The error bar represents 95 per cent confidence interval for the solid curves. The occurrence date of earthquakes is written in each panel. Observed radial component seismogram is drawn by thin black curve on the background of each panel, where the amplitude is arbitrary. The vertical dashed line represents *S*-wave onset time.

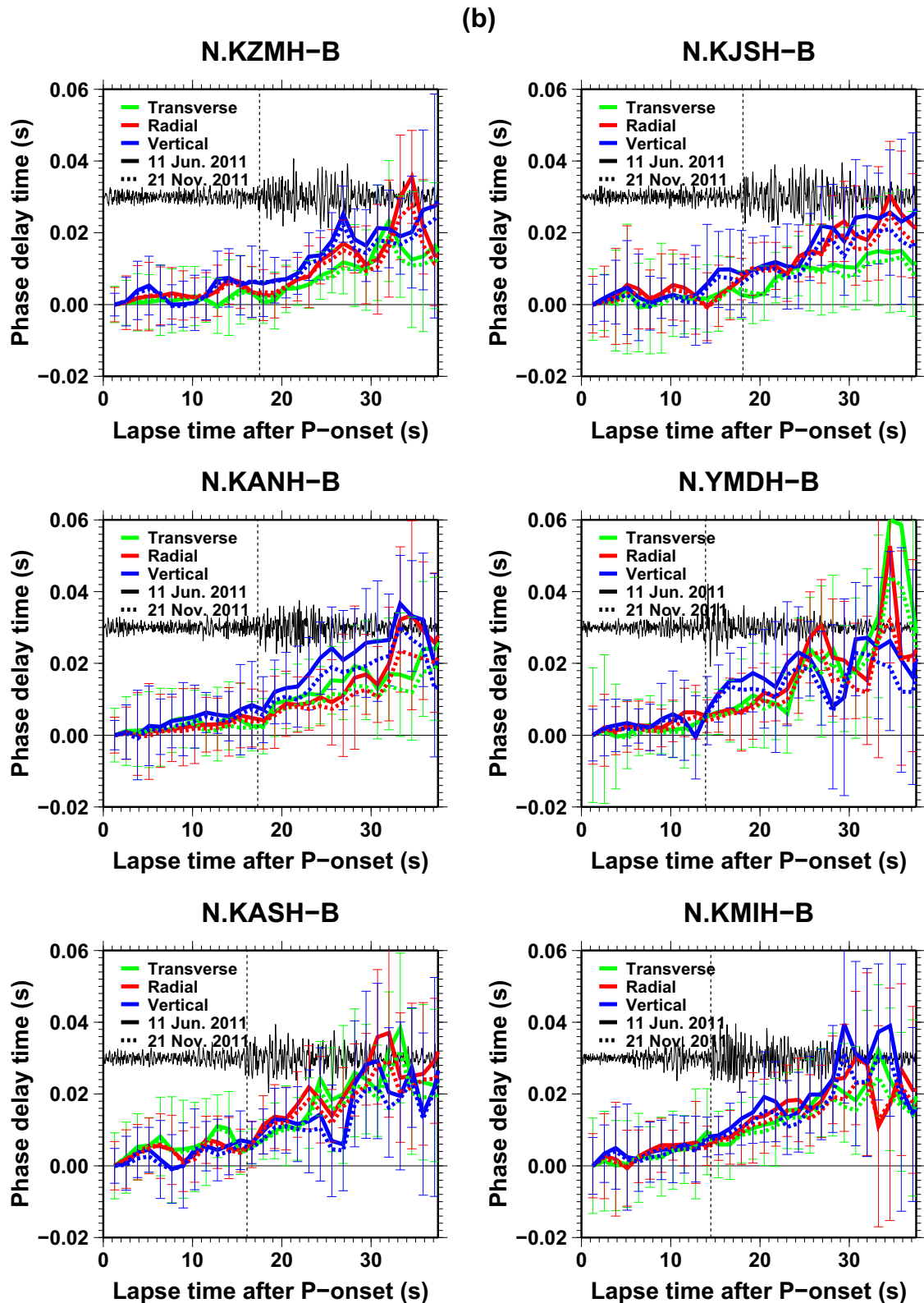


Figure 3. (Continued.)

In Figs 4(a) and (b), we also show the V_S and V_P reduction ratios detected at the subsurface down to a few hundred meters depth, respectively, by a different colour scale (triangles). Their 95 per cent confidence intervals are shown in Figs 5(a) and (b), respectively. These values are measured by applying deconvolution analysis to

KiK-net vertical array records (Sawazaki & Snieder 2013). The V_S at the shallow subsurface reduces at many stations up to 6 per cent within 1 month after the main shock, and it continues to recover for 1 yr. Spatial correlation between the V_S reduction ratio at the shallow subsurface and the apparent velocity reduction ratio obtained in this

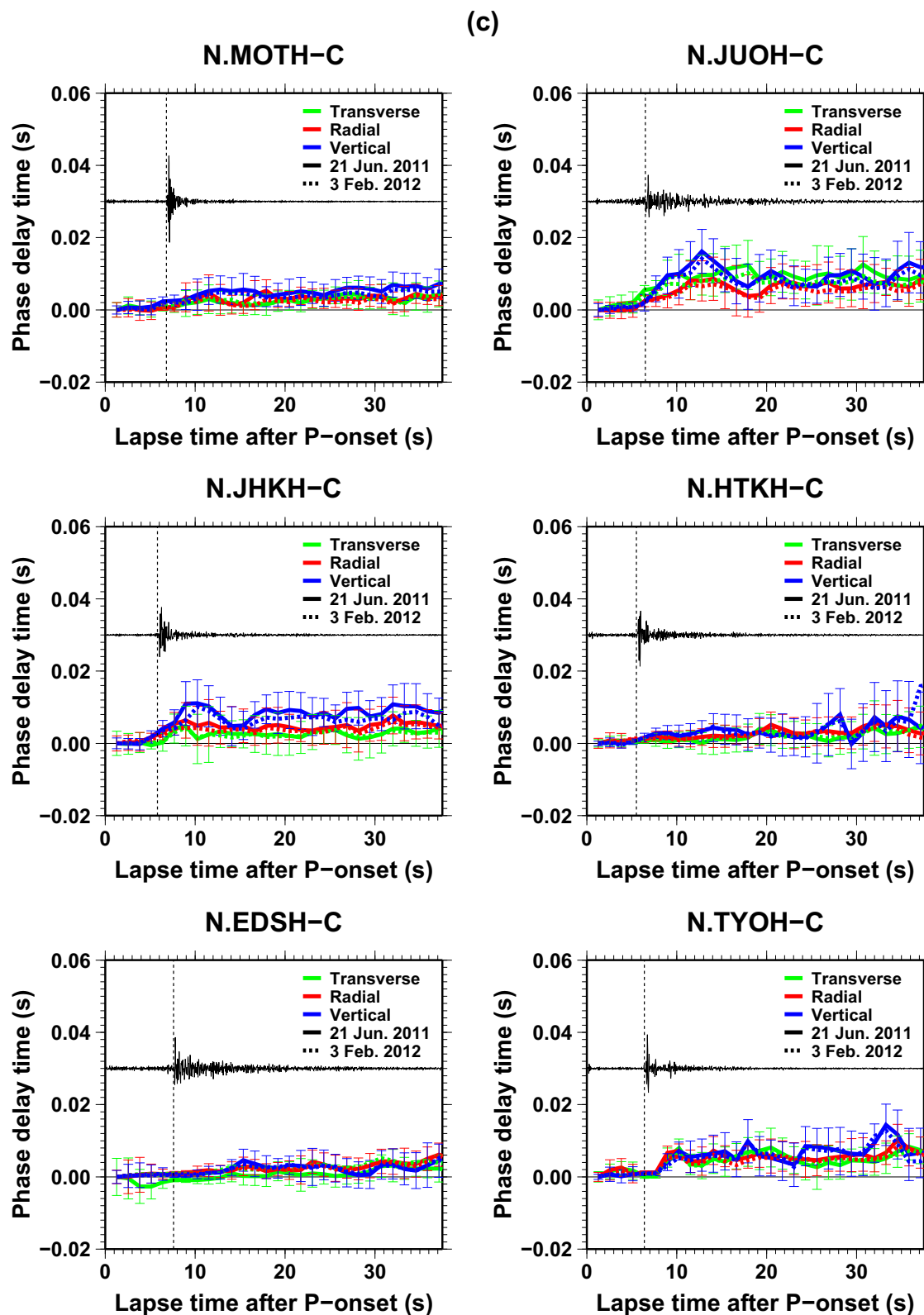


Figure 3. (Continued.)

study is confirmed in the period of 0–1 month after the main shock, while it becomes less clear at the later lapse times. On the other hand, V_p at the shallow subsurface shows much smaller velocity reductions, and its recovery process is not clearly observed.

Fig. 6 demonstrates a direct comparison between the V_S change ratio at the shallow subsurface down to 300 m depth measured at Hi-net station N.YMAH (red triangle in Fig. 6a) and the apparent velocity change ratio measured for S -wave time windows at three

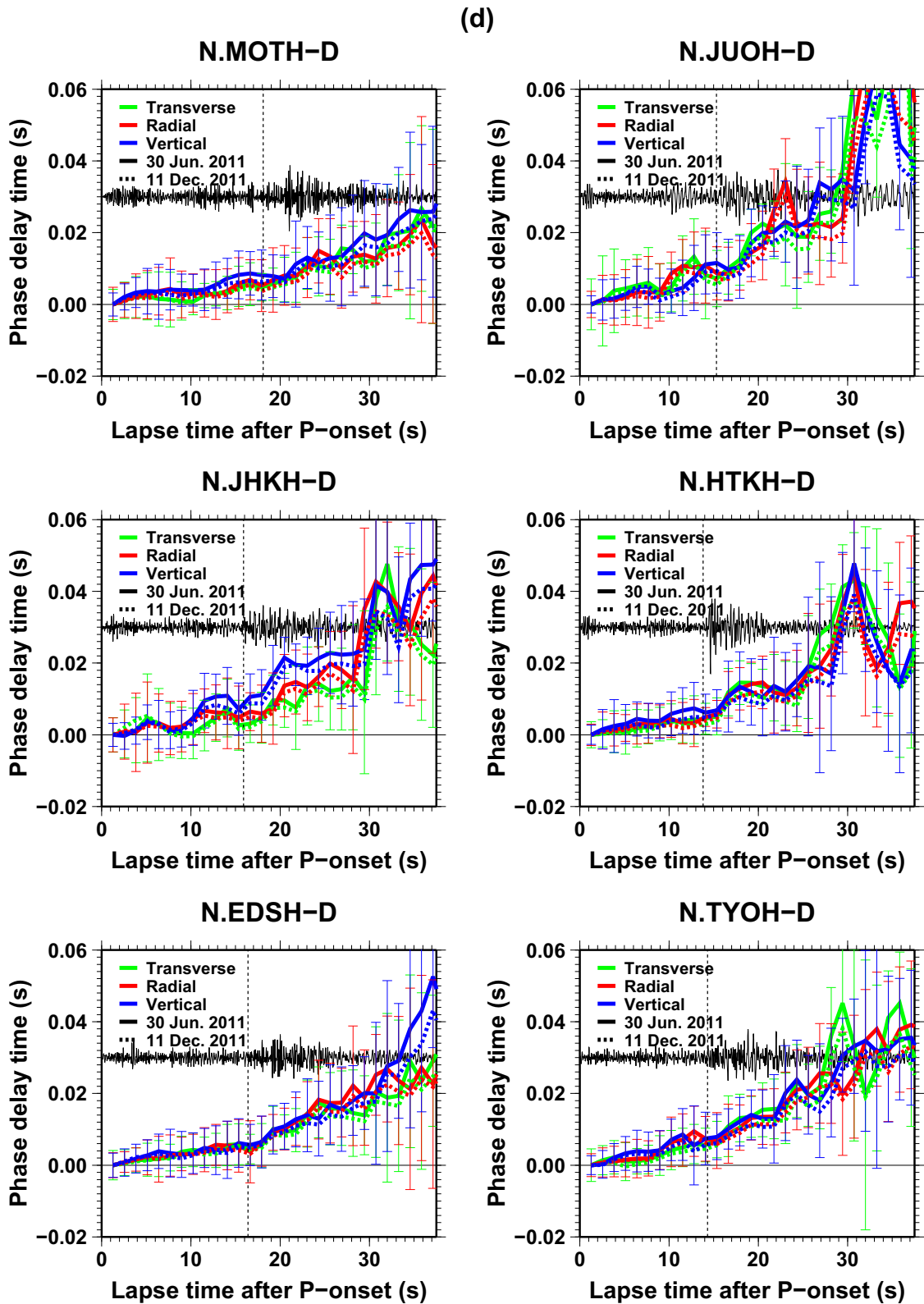


Figure 3. (Continued.)

areas (coloured rectangles in Fig. 6a). The station N.YMAH is collocated with KiK-net station IBRH16, which is referred in fig. 5 of Sawazaki & Snieder (2013). The measured apparent velocity reduction ratio is much smaller than the V_S reduction ratio detected at

the shallow subsurface. This difference indicates that the velocity reduction is essentially concentrated at the shallow subsurface. The offshore area (blue) shows the largest apparent velocity reduction among the three areas for all time periods. The apparent velocities

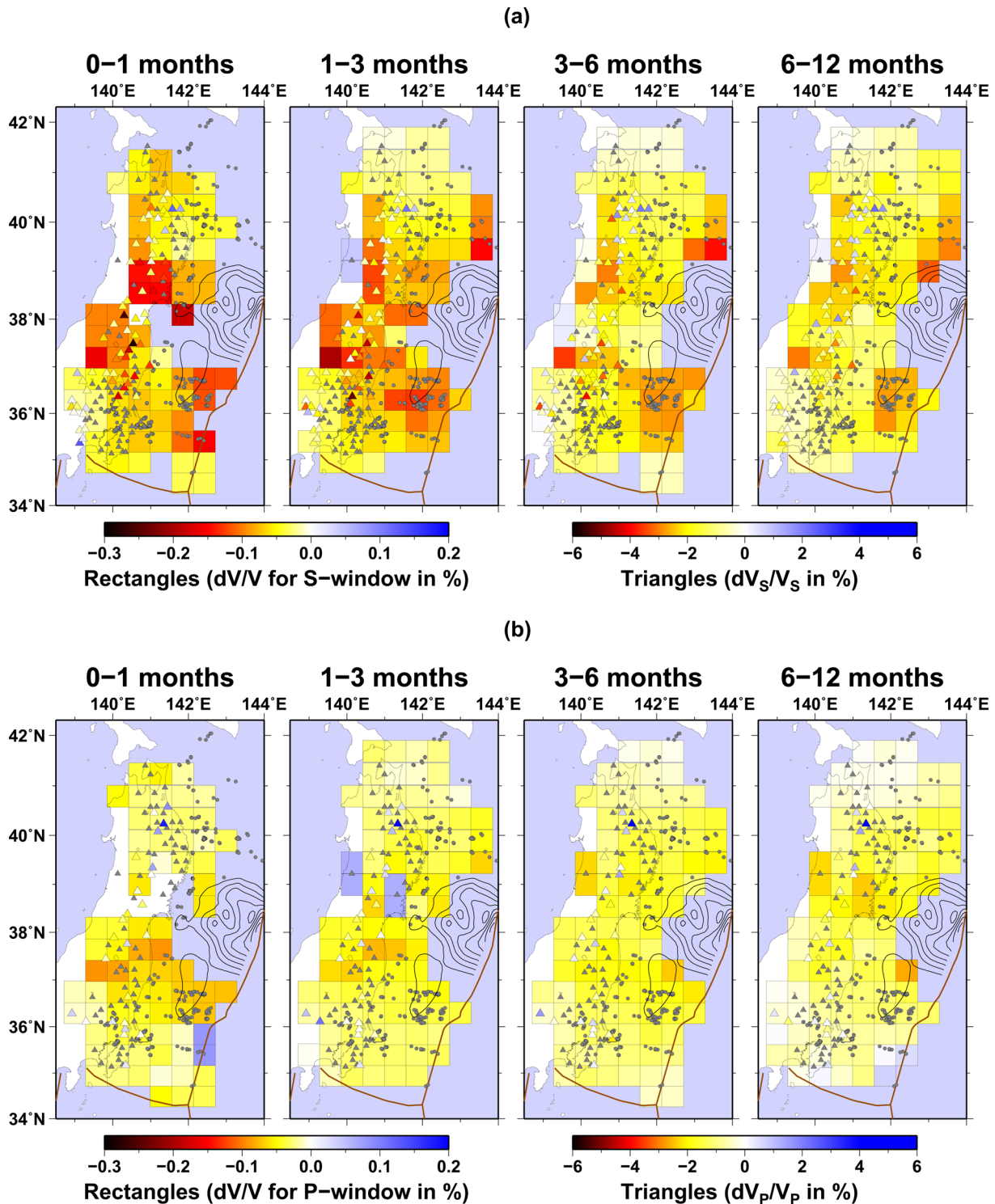


Figure 4. The colour of rectangles represents apparent velocity change ratio after the Tohoku earthquake measured using (a) S -wave and (b) P -wave time windows. The vertical component is used for the mapping. Colour scale is shown on the left bottom in each figure. The colour of triangles represents (a) V_S and (b) V_P change ratios detected in the shallow subsurface by Sawazaki & Snieder (2013), where its colour scale is shown on the right bottom in each figure. Observed time period is divided into 0–1, 1–3, 3–6 and 6–12 months after the Tohoku earthquake. The black contour curves represent slip distribution of the Tohoku earthquake by 10 m slip interval following Iinuma *et al.* (2012).

show small recoveries within 1 yr, while the V_S at the shallow subsurface almost recovers within the same time period. This difference in recovery speed indicates that velocity at the deeper zone recovers more slowly compared to that at the shallower zone.

5 FINITE DIFFERENCE SIMULATION

To examine the sensitivity of the observed phase delay curve to spatial variations of velocity change, we perform a 2-D FD wave propagation simulation. We consider a realistic wave scattering

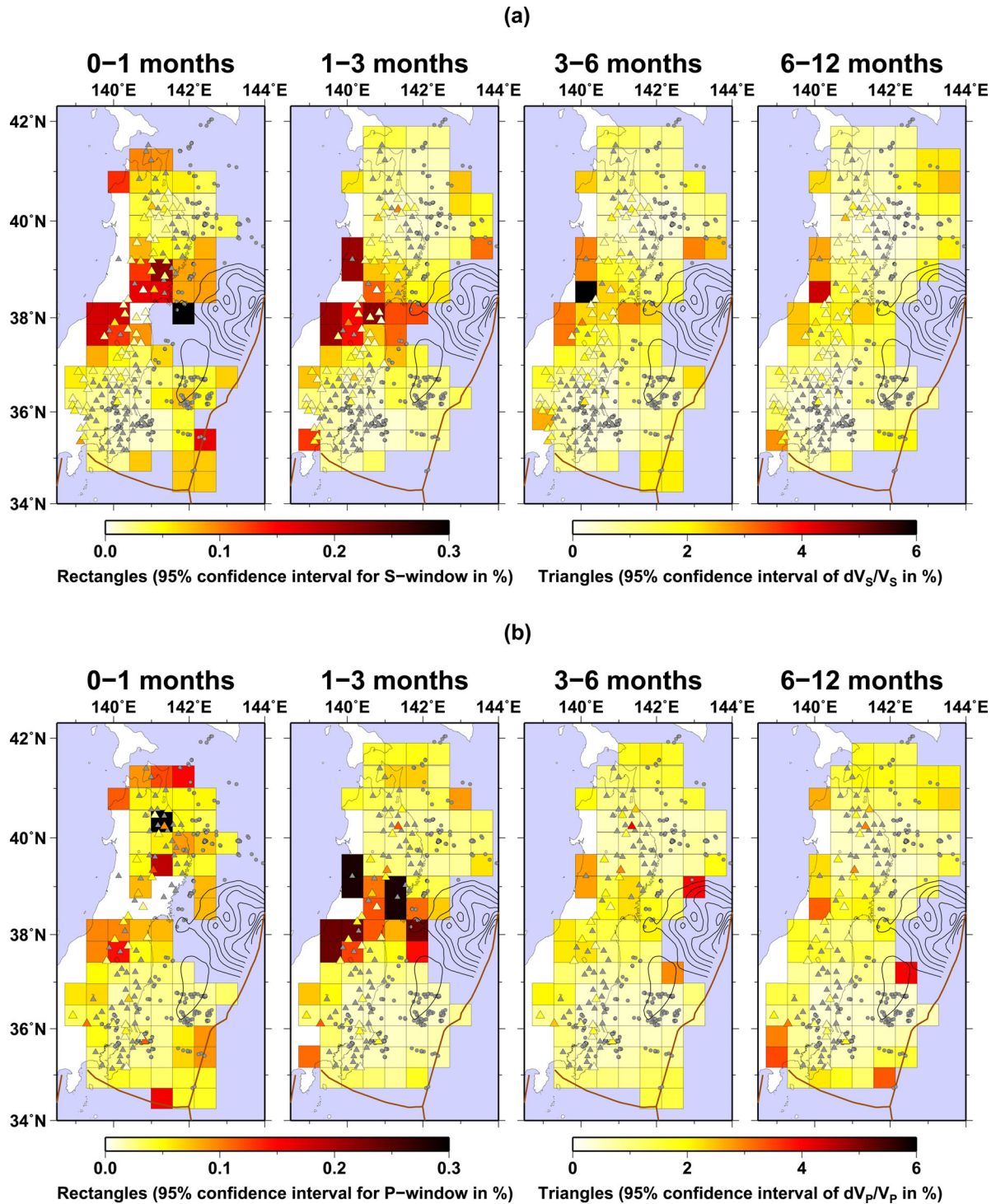


Figure 5. The colour of rectangles represents 95 per cent confidence interval of the apparent velocity change ratio after the Tohoku earthquake measured using (a) S -wave and (b) P -wave time windows. The vertical component is used for the mapping. Colour scale is shown on the left bottom in each figure. The colour of triangles represents 95 per cent confidence interval of (a) V_S and (b) V_P change ratios detected in the shallow subsurface by Sawazaki & Snieder (2013), where its colour scale is shown on the right bottom in each figure. Observed time period is divided into 0–1, 1–3, 3–6 and 6–12 months after the Tohoku earthquake. The black contour curves represent slip distribution of the Tohoku earthquake by 10 m slip interval following Iinuma *et al.* (2012).

process employing a depth-dependent velocity structure and random inhomogeneous media. Due to the limitation of computation time, we do not perform 3-D simulations. Therefore, we do not examine the sensitivity to V_P and V_S changes separately because partitions of P - and S -wave energies are much different between 2-D and 3-D media (according to Weaver (1982) and Sánchez-Sesma

& Campillo (2006), the ratio of S -wave energy with respect to P -wave energy is 3.0 and 10.4 for 2-D and 3-D Poisson's media in equipartition state, respectively).

The phase delay can be excited not only by a change of medium velocity but also by a displacement of source location after the Tohoku earthquake. To examine how the displacement of source

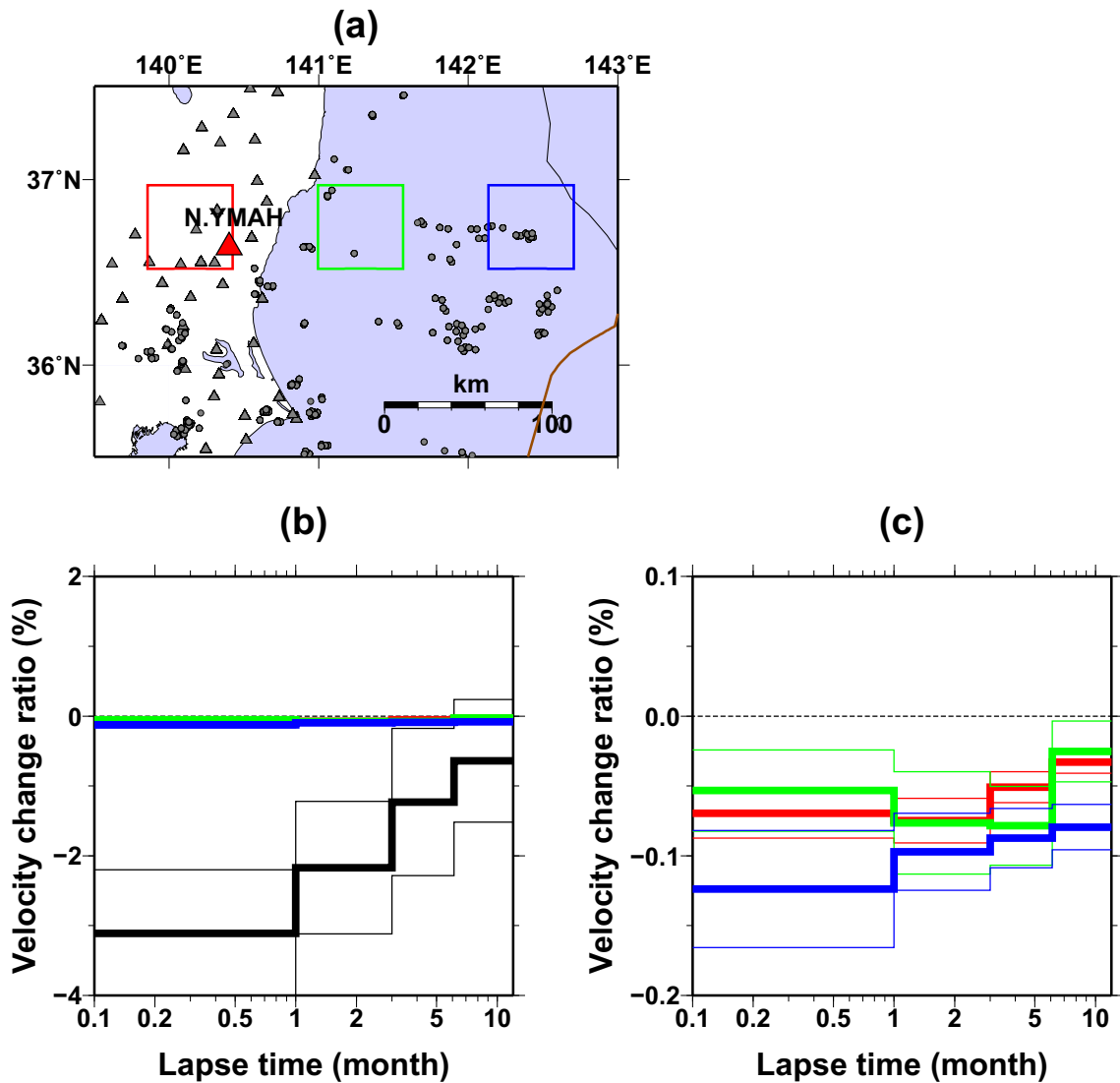


Figure 6. (a) Map of Hi-net station N.YMAH (red triangle. KiK-net code is IBRH16) and subareas (coloured rectangles). (b) Time lapse change in V_S change ratio detected by Sawazaki & Snieder (2013) (black thick line) and apparent velocity change ratios calculated for S -wave time window (coloured thick lines), where colours of the lines correspond to the colours of the three subareas shown in Fig. 6a. Fig. 6c represents magnification of Fig. 6b at velocity change ratio from -0.2 to 0.1 per cent. The thin lines represent 95 per cent confidence interval.

location affects the observed phase delay curve, we also conduct an FD simulation for slightly different source locations.

5.1 Simulation setting

Fig. 7 shows an example of used velocity profile and locations of source (focal mechanisms) and receiver (triangle) used in our FD simulation. The sources and receiver location are set considering the geometry of north area shown in Fig. 1(b), where station N.KANH is selected as the target station. Since this station is located near the cross-section along the clusters A and B, radial and vertical components recorded at this station are directly comparable to those simulated using 2-D medium. A double-couple line source with a dip angle of 22.5° is adopted considering the focal mechanism of earthquakes occurring on the boundary between the Pacific and the overlying plates. A Küpper wavelet with the dominant frequency of 3 Hz is used as a source time function, where frequency range used in the MTWCA (1–10 Hz) is considered. The model covers a

region of 360 km horizontally and 180 km in depth, with a discrete grid size of 75 m. Reflective and absorbing boundary conditions are employed for the top free surface and for the other three boundaries of the computation area, respectively, where the particle velocity near the absorbing boundary is forced to attenuate following an exponential form

$$\exp[-\alpha^2 (J - j)^2] \quad (j = 1, 2, \dots, J), \quad (9)$$

where $\alpha = 0.02$ and $J = 50$ is adopted by trial and error.

The velocity profile modified from Nakajima *et al.* (2001) and the well-log data provided by NIED are used as the background 1-D velocity structure for below and above 1 km depth, respectively. The mass density ρ is given by $\rho = 310V_p^{0.25}$ following Gardner *et al.* (1974). The quality factor Q is given as a function of depth as shown in Fig. 8, which is common for both P and S waves for a

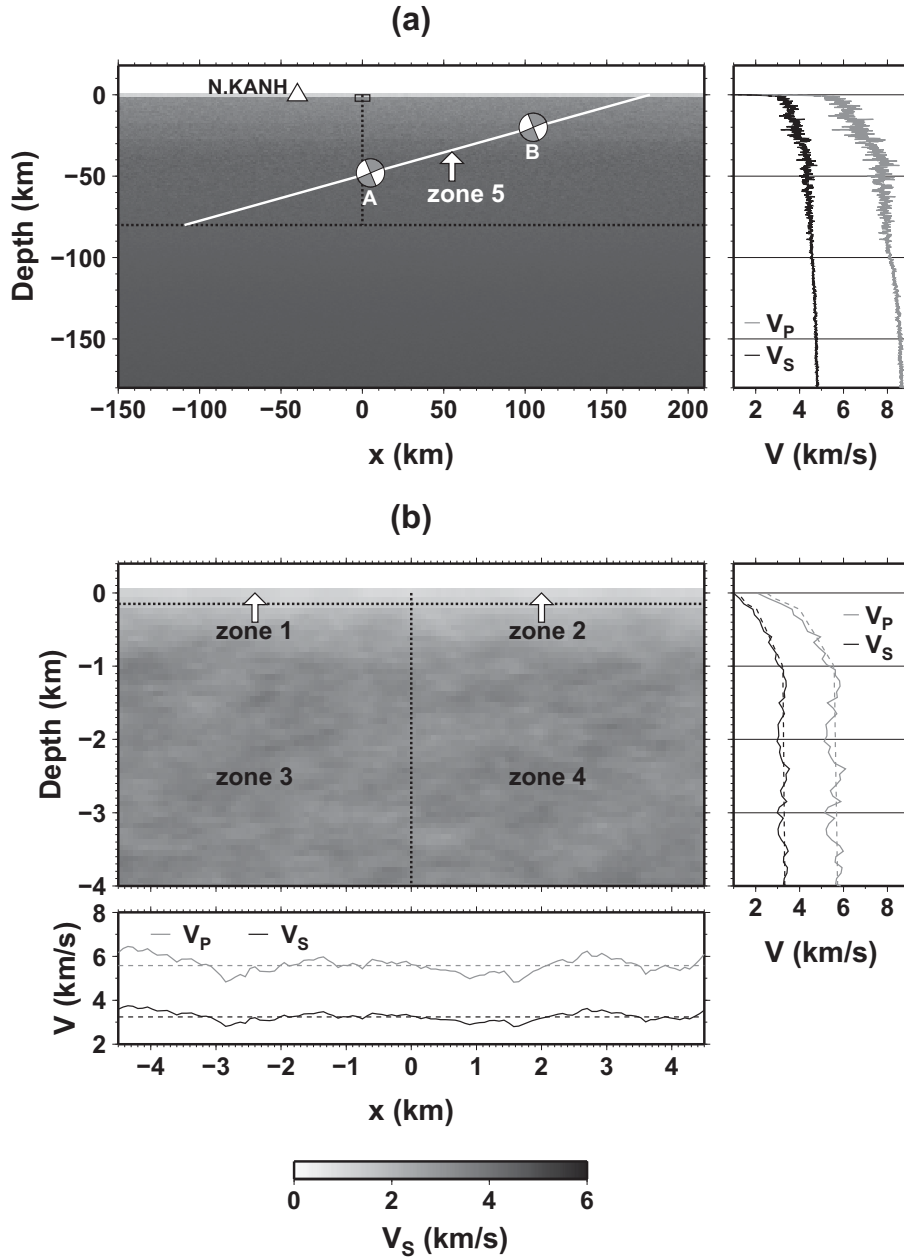


Figure 7. (a) 2-D velocity profile and locations of sources (focal mechanism) and receiver (triangle) used in FD simulation. The vertical cross sections of V_P (grey curve) and V_S (black curve) are shown in the right panel, where the dashed lines are background 1-D velocity profile by Nakajima *et al.* (2001). The white line indicates the approximate faulting zone with the thickness of 150 m (zone 5), where the velocity is reduced in the numerical simulation. (b) Magnification of Fig. 5(a) at ranges of $-4.5 \text{ km} < x < 4.5 \text{ km}$ and $-4 \text{ km} < \text{Depth}$. The vertical and horizontal cross sections are shown in the right and bottom panels, respectively. The zones from 1 to 4 represent the zones where a partial velocity change is applied in the numerical simulation.

technical reason. The autocorrelation function of fractional velocity fluctuation is 2-D exponential-type given by

$$R(x, z) = \varepsilon(z)^2 \exp\left(-\sqrt{\frac{x^2}{a_x^2} + \frac{z^2}{a_z^2}}\right), \quad (10)$$

where ε , a_x and a_z represent rms fractional velocity fluctuation and correlation distances for horizontal and vertical scales, respectively. We choose non-isotropic random elastic media with $a_x = 3 \text{ km}$ and $a_z = 1 \text{ km}$ (e.g. Furumura & Kennet 2005; Sato 2008). ε is given as a function of depth as shown in Fig. 9, which accounts for strong and weak heterogeneities in the crust and in the upper mantle, respectively (e.g. Margerin *et al.* 2000). We assume that

the value of ε is common for V_P and V_S , and 0.8ε for mass density (e.g. Sato *et al.* 2012). We checked that the numerical instability and numerical dispersion do not emerge significantly for the given medium and dominant frequency.

5.2 Sensitivity to partial velocity change

Using the velocity structure described above as the reference medium and partially reducing velocities of five zones (shown in Fig. 6), we compute phase delay curves for the selected source-station pairs. The computation area is laterally separated into west (zones 1 and 3) and east (zones 2 and 4) of the coastline, and is

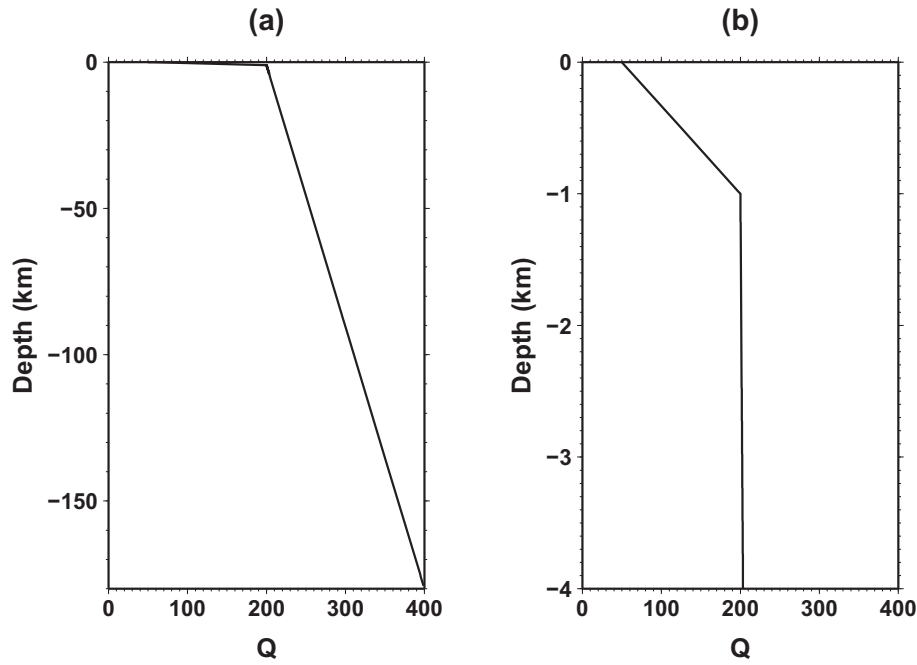


Figure 8. (a) Depth-profile of quality factor Q used in FD simulation. (b) Magnification of Fig. 8(a) at top 4 km.

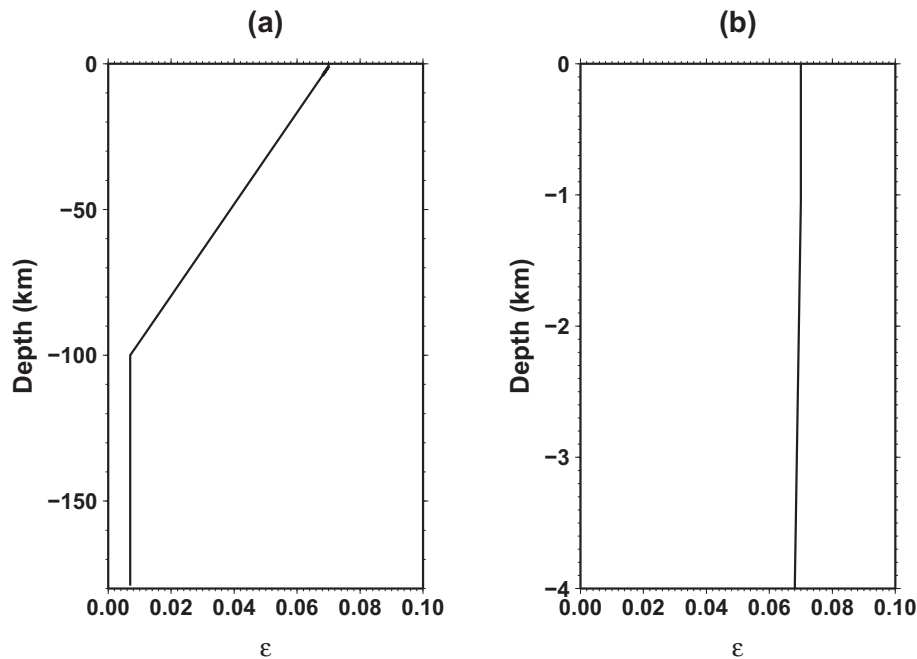


Figure 9. (a) Depth-profile of rms fractional velocity fluctuation ε used in FD simulation. (b) Magnification of Fig. 9(a) at top 4 km.

vertically separated into above (zones 1 and 2) and below (zones 3 and 4) 150 m depth. Here, 150 m is an approximate installation depth of the borehole bottom sensor of Hi-net, above which Sawazaki & Snieder (2013) detected velocity change ratio through the deconvolution analysis of KiK-net vertical array data. The depth limit of zones 3 and 4 is set to 80 km, below which the faulting zone of the Tohoku earthquake does not penetrate. We also partially reduce the velocity of faulting zone along the plate boundary with the thickness of 150 m (zone 5). Since KiK-net and Hi-net are terrestrial seismograph networks, velocity changes at zones 2, 3,

4 and 5 have not been examined well in previous studies. Applying a 1 per cent velocity reduction to zones 1, 2 and 5, and applying a 0.1 per cent velocity reduction to zones 3 and 4 individually, and using 10 different seeds of random inhomogeneous media, we compute 10 phase delay curves for the five partial velocity reductions. Here, the percentage of velocity reduction is common for both V_p and V_s .

The average and the 95 percent confidence interval of the 10 simulated phase delay curves are shown in Fig. 10, where curves for the sources A and B are drawn in Figs 10(a) and (b),

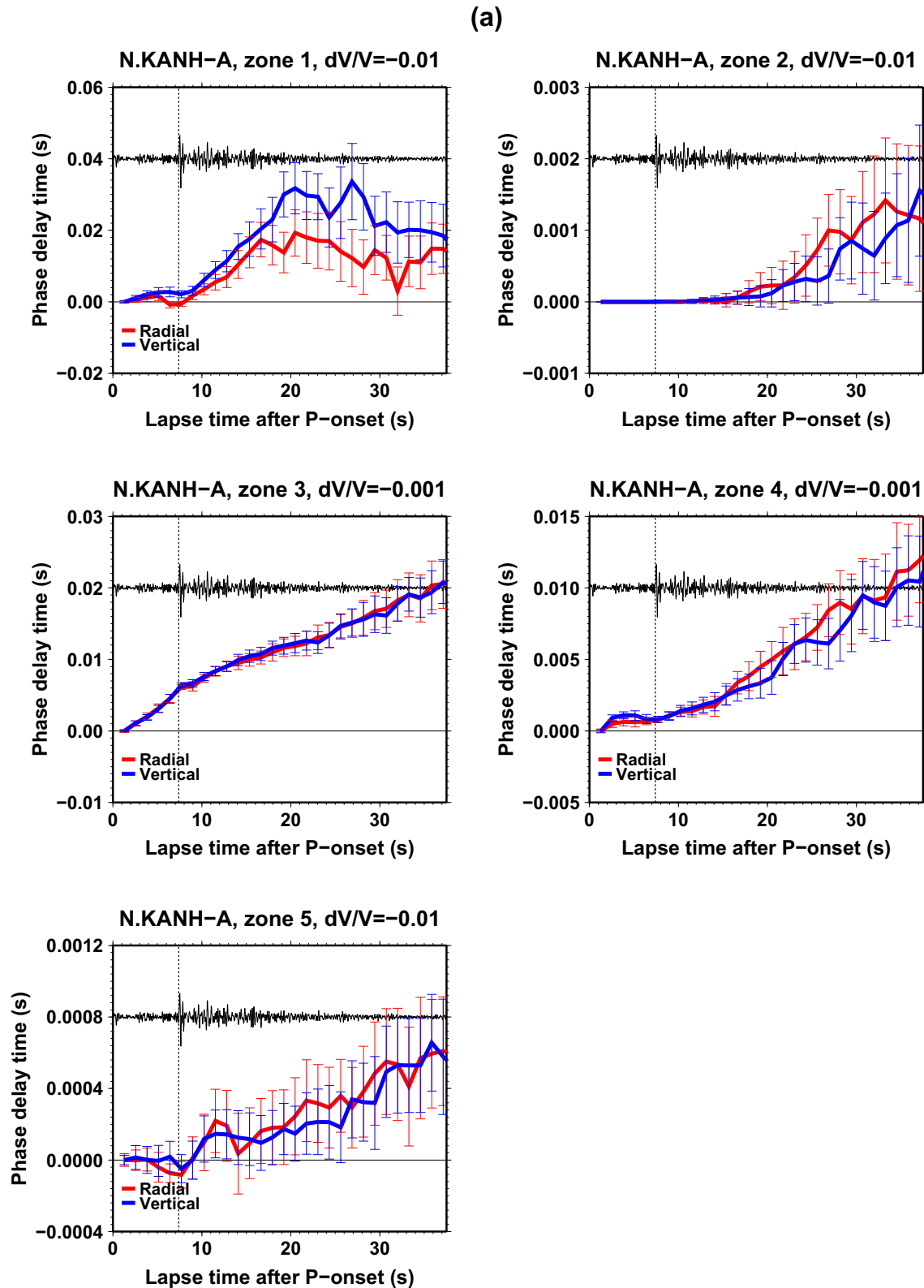


Figure 10. Simulated phase delay curves at station N.KANH for clusters (a) A and (b) B. The five panels in each figure represent phase delay curves calculated for a 1 per cent partial velocity reduction at zones 1, 2 and 5, and that for a 0.1 per cent velocity reduction at zones 3 and 4. The red and blue curves represent radial and vertical components, respectively. The error bar represents 95 per cent confidence interval calculated from 10 simulated phase delay curves for 10 seeds of random inhomogeneous media. Simulated seismograms (radial component) are drawn by thin black curves on the background of each panel, where the amplitude is arbitrary. The vertical dashed line represents *S*-wave onset time.

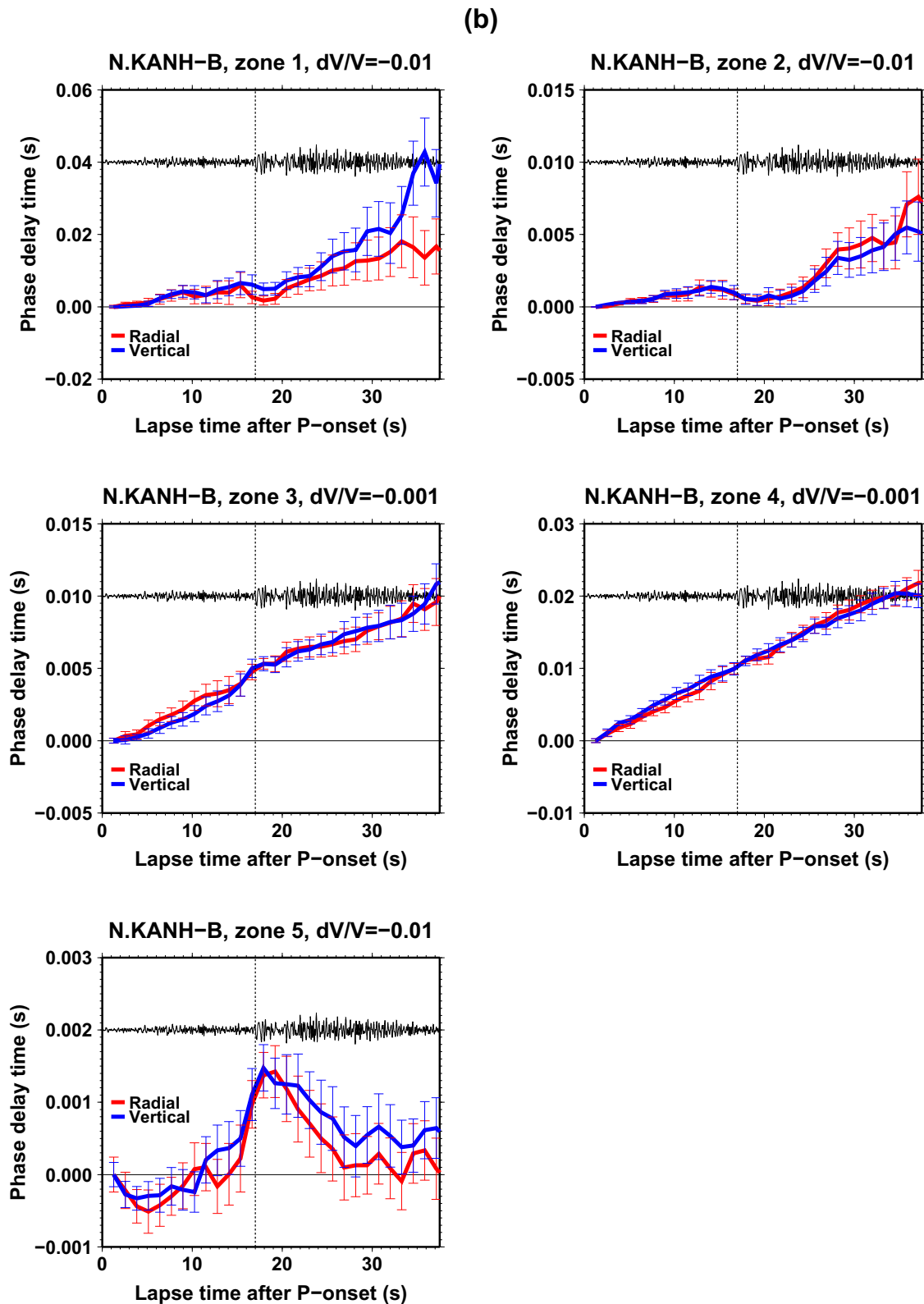


Figure 10. (Continued.)

respectively. When a 1 per cent velocity reduction is applied at zone 1, the phase delay for the near-coast source A starts to increase after the *S*-wave arrival time and becomes almost constant for the later *S*-coda. The phase delay is larger for the vertical component than for the radial component. We interpret this by the *S*-wave being

trapped by the shallow low-velocity layers and the Rayleigh-wave that are sensitive to the velocity reduction in the shallow subsurface. Because the energy of these horizontally propagating waves is more dominant in the vertical component than in the radial component, the phase delay should become larger for the vertical component.

For the later *S*-coda, back-scattered waves that propagate through the deeper zone become dominant. Since they are not so sensitive to the velocity reduction at zone 1, the later *S*-coda does not show significant phase delays.

A 1 per cent velocity reduction applied at zone 2 excites very small phase delays because waves rarely propagate through zone 2. Therefore, the pair of source A and station N.KANH hardly constrains the velocity change at zone 2. When a 0.1 per cent velocity reduction is applied at zones 3 and 4, the phase delay starts to increase from the *P*-wave onset time and it does not show significant difference between the radial and vertical components. Probably, body waves that propagate through the deep zones are randomly scattered and they do not generate specific polarizations. The phase delay curve is almost insensitive to the 1 per cent velocity reduction at faulting zone (zone 5).

For the offshore source B (Fig. 10b), a 1 per cent velocity reduction applied at zone 1 excites gentle and sharp phase delay slopes at the *P*- and *S*-wave time windows, respectively. Here again, the phase delay time is larger for the vertical component than for the radial component. When a 1 per cent velocity reduction is applied at zone 2, the phase delay becomes larger than the case of source A because source B is located at offshore, shallower zone. However, the phase delay is still less sensitive compared to the case of velocity reduction at zone 1. When a 0.1 per cent velocity reduction is applied at zones 3 and 4, the phase delay increases almost linearly from the *P*-wave onset time, and there are no differences between the radial and vertical components. For the 1 per cent velocity reduction at zone 5, the phase delay reaches to the maximum around the direct *S*-wave onset time and the slope becomes negative at *S*-coda (apparent velocity increases).

Comparison of the observed (Fig. 3) and the synthesized (Fig. 10) phase delay curves indicates that the 1 per cent velocity reduction at zone 1 best explains the observed phase delay curves in terms of both shape and amount of phase delay. This 1 per cent velocity reduction is consistent with the V_S reduction at the shallow subsurface detected by Sawazaki & Snieder (2013) (see Fig. 4a).

Contribution of other three zones to the observed phase delay curves is interpreted as follows. Because zone 2 is close to large slip area of the main shock and thereby ground motion excited there should be strong, velocity reduction at zone 2 could be larger than that at zone 1. Also, unlike the terrestrial area, sediments on the seafloor are completely saturated by water and shear strength in the marine sediments may be more sensitive to strong ground motion than that on the land. However, the velocity reduction at zone 2 cannot be constrained well in our analysis because the phase delay curve is not sensitive to the velocity change in this zone.

Because the shape of observed phase delay curve is not similar to that of simulated curves for the velocity reductions at zones 3 and 4, we think velocity reduction at these zones should be much smaller than 0.1 per cent. However, as shown in Figs 4(a) and 6, the spatial correlation between the shallow V_S change ratio and the apparent velocity change ratio is more clearly observed in the earlier lapse times, and the apparent velocity change ratio recovers more slowly compared to V_S at the shallow subsurface. These observations indicate that the velocity change at the shallow zones alone cannot fully explain the observed phase delay curve. We think the velocity change at the deep zones is hardly confirmed from the observed phase delay curves at early lapse times (before 1 month), while its contribution gradually stands out as the velocity of shallow zone recovers at long lapse times (over 1 yr). Unlike in the shallow zone, damage by strong shaking would not be significant in the deep zone because surrounding rock is very stiff. Instead, a static strain

change associated with the main shock faulting and the post-seismic deformation should bring more damage to the rock at this depth.

For the velocity change at zone 5, even the velocity reduction as large as 1 per cent hardly contributes to the observed phase delay curves. This means that the velocity change along the faulting zone is hardly detectable for the Tohoku earthquake and it is difficult to constrain the velocity changes at this zone.

5.3 Sensitivity to displacement of source location

In addition to the partial velocity change, displacement of source location also contributes to the phase delay. Recently, Uchida *et al.* (2015) applied the double-difference (DD) relocation technique to waveforms of Kamaishi repeating cluster (close to cluster A in Fig. 1), and found that source location of many repeating earthquakes moved toward west after the Tohoku earthquake, except for some large events that have large slip area. The direction of source displacement and source mechanism indicate that the source moved along the direction of subduction on the plate boundary. Following their result, we perform a numerical simulation by moving the source locations A and B towards west by 150 m and deeper zone by 75 m, and calculate phase delay curves using waveform pairs before and after the displacement of the source.

Figs 11(a) and (b) show the simulated phase delay curves for the displacement of sources A and B, respectively. Partial velocity reduction is not applied in this simulation. For the displacement of source A, a small phase delay appears at the later *S*-coda. For the displacement of source B, on the other hand, a phase ‘advance’ (negative phase delay) appears at the direct *S*-wave onset time and the phase delay gradually increases for the *S*-coda. There is no significant difference in phase delay time between the radial and the vertical components.

The phase advance appeared at the *S*-wave onset time for the source B indicates a decrease of *P*–*S* traveltime difference after the displacement of the source. The $150\text{ m} \times 75\text{ m}$ source displacement causes $0.168 \cos\theta(1/V_S - 1/V_P)$ s decrease in *P*–*S* traveltime difference, where the units of V_S and V_P is km s^{-1} and θ is the angle between the take-off direction from the source to the station and the direction of source displacement. The obtained phase advance of 0.016 s for the source B agrees with the calculated decrease in *P*–*S* traveltime difference if $V_S = 3.8\text{ km s}^{-1}$, $V_P = 6.7\text{ km s}^{-1}$ and $\theta = 30^\circ$ are reasonably assumed. For the source A, the obtained phase advance of 0.004 s is well explained if $V_S = 4.4\text{ km s}^{-1}$, $V_P = 7.8\text{ km s}^{-1}$ and $\theta = 75^\circ$ are assumed.

For the later *S*-coda, multiply scattered waves lose information of source location and phase delay becomes gradually invisible (Snieder & Vrijlandt 2005). Therefore, the difference between the phase delay time at later *S*-coda and that at direct *P*-wave asymptotes to negative value of the *P*-wave traveltime difference before and after the source displacement. For the applied westward source displacement, *P*-wave traveltime decreases because of the shortening of ray path. This is the reason why the phase gradually asymptotes to positive delay time at later *S*-coda in Fig. 11.

In this way, the numerical simulation predicts phase advance at direct *S*-wave onset time and gradual asymptotes to a positive delay time at later *S*-coda especially for the source B. Of course, this tendency is opposite if the source moves toward the east and shallower zone. However, for both westward and eastward displacement, such phase changes predicted from Fig. 11(b) are not observed for any stations in Fig. 3(b). For source A, the shape of the phase delay curve predicted from Fig. 11(a) is similar to the observed phase

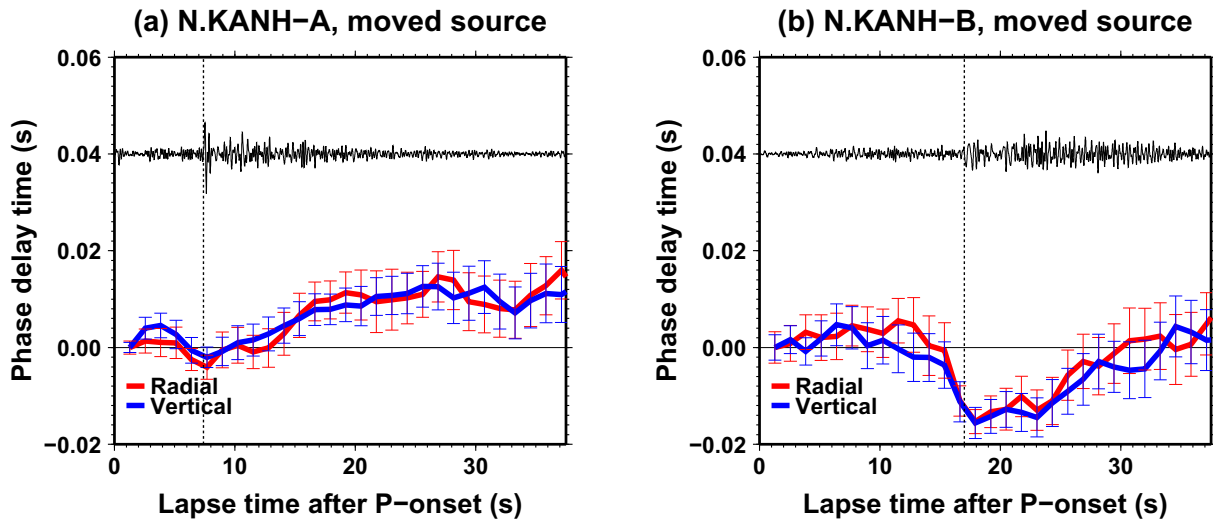


Figure 11. Simulated phase delay curves at station N.KANH for clusters (a) A and (b) B. The phase delay curves are calculated for a displacement of source location toward west by 150 m and deeper zone by 75 m. The red and blue curves represent radial and vertical components, respectively. The error bar represents 95 per cent confidence interval calculated from 10 simulated phase delay curves for 10 seeds of random inhomogeneous media. Simulated seismograms (radial component) are drawn by thin black curves on the background of each panel, where the amplitude is arbitrary. The vertical dashed line represents S -wave onset time.

delay curves shown in Fig. 3(a). However, the simulated phase delay curve does not explain the difference in radial and transverse components detected in the observation. In conclusion, the displacement of source before and after the main shock is not likely the primary cause of the observed phase delays.

6 DISCUSSION

6.1 Velocity change caused by static strain change

In the previous section, we have confirmed that about 1 per cent velocity reduction at the top 150 m depth is largely responsible to the observed phase delay curves. The velocity reduction at the deeper zone is considered to be much smaller than 0.1 per cent, and this reduction is still in a recovery process 1 yr after the main shock. However, is this small velocity reduction at the deeper zone consistent with observed large-scale deformation by the Tohoku earthquake? In this section, we evaluate possible velocity changes due to the static strain change by the Tohoku earthquake, and discuss whether the estimated velocity reduction ratio, ‘much smaller than 0.1 per cent’, is reasonable or not. To evaluate velocity change due to the static strain change, we use the finite deformation theory of Murnaghan (1967) and the slip model of Iinuma *et al.* (2012) for the Tohoku earthquake.

The constitutive relation between stress and strain becomes non-linear if polynomial terms are not negligible under a large strain. Considering the second order term with respect to the strain tensor ε , the stress tensor τ is given by

$$\tau_{ij} \approx (C_{ijkl}^0 + C_{ijklmn}\varepsilon_{mn})\varepsilon_{kl}, \quad (11)$$

where C_{ijkl}^0 is elastic tensor of reference rock before applying the strain. The change of the elastic tensor with respect to the strain change $\Delta\varepsilon_{mn}$ is given by

$$\Delta C_{\alpha\beta} = C_{\alpha\beta\gamma}\Delta\varepsilon_{\gamma}, \quad (12)$$

where we use the symmetry of stress and strain tensors ($ij = ji = \alpha$, $kl = lk = \beta$ and $mn = nm = \gamma$). $C_{\alpha\beta\gamma}$ is called ‘the third order elastic

(TOE) tensor’ in crystallography (e.g. Hearmon 1953). If the TOE tensor is invariant with respect to any coordinate transformation, the number of independent component of the isotropic TOE tensor is reduced to three; C_{111} , C_{112} and C_{123} .

When the reference medium is isotropic and the elastic constants are $C_{11}^0 = \lambda + 2\mu$ and $C_{44}^0 = \mu$, where λ and μ are the Lamé’s constant, the V_P and V_S change ratios associated with the applied strain change ε are given by

$$\begin{aligned} \frac{\Delta V_{P_i}}{V_{P_i}^0} &= \frac{1}{2C_{11}^0} [C_{111}\varepsilon_i + C_{112}(\varepsilon_j + \varepsilon_k)] + \frac{1}{2} \sum_{l=1}^3 \varepsilon_l \\ \frac{\Delta V_{S_{ij}}}{V_{S_{ij}}^0} &= \frac{\Delta V_{S_{ji}}}{V_{S_{ji}}^0} = \frac{1}{2C_{44}^0} [C_{144}\varepsilon_k + C_{155}(\varepsilon_i + \varepsilon_j)] + \frac{1}{2} \sum_{l=1}^3 \varepsilon_l, \end{aligned} \quad (13)$$

where

$$\begin{aligned} C_{144} &= \frac{1}{2}(C_{112} - C_{123}) \\ C_{155} &= \frac{1}{4}(C_{111} - C_{112}). \end{aligned} \quad (14)$$

Here the subscripts i, j and k represent directions of three principal axes of applied strain tensor which satisfies $i \neq j, j \neq k$ and $k \neq i$. V_{P_i} represents P -wave velocity that propagates along i -direction, and $V_{S_{ij}}$ represents S -wave velocity that propagates along i -direction polarizing along j -direction. The derivation of eq. (13) is summarized in Appendix B.

Fig. 12 shows the excited maximum principal strain change (red arrows) due to the coseismic slip of the Tohoku earthquake and its 1-month post-seismic deformation at depths of 5, 25, 45 and 65 km. The maximum principal strain change larger than 5×10^{-4} is not shown because of visibility of the figure. The slip distribution model of Iinuma *et al.* (2012) and simulation code by Okada (1992) are used to calculate the static strain change. The slip model of Iinuma *et al.* (2012) is based not only on the terrestrial GPS observations but also on the seafloor GPS/Acoustic ranging (Kido *et al.* 2011; Sato *et al.* 2011) and the Ocean Bottom Pressure gouges. The

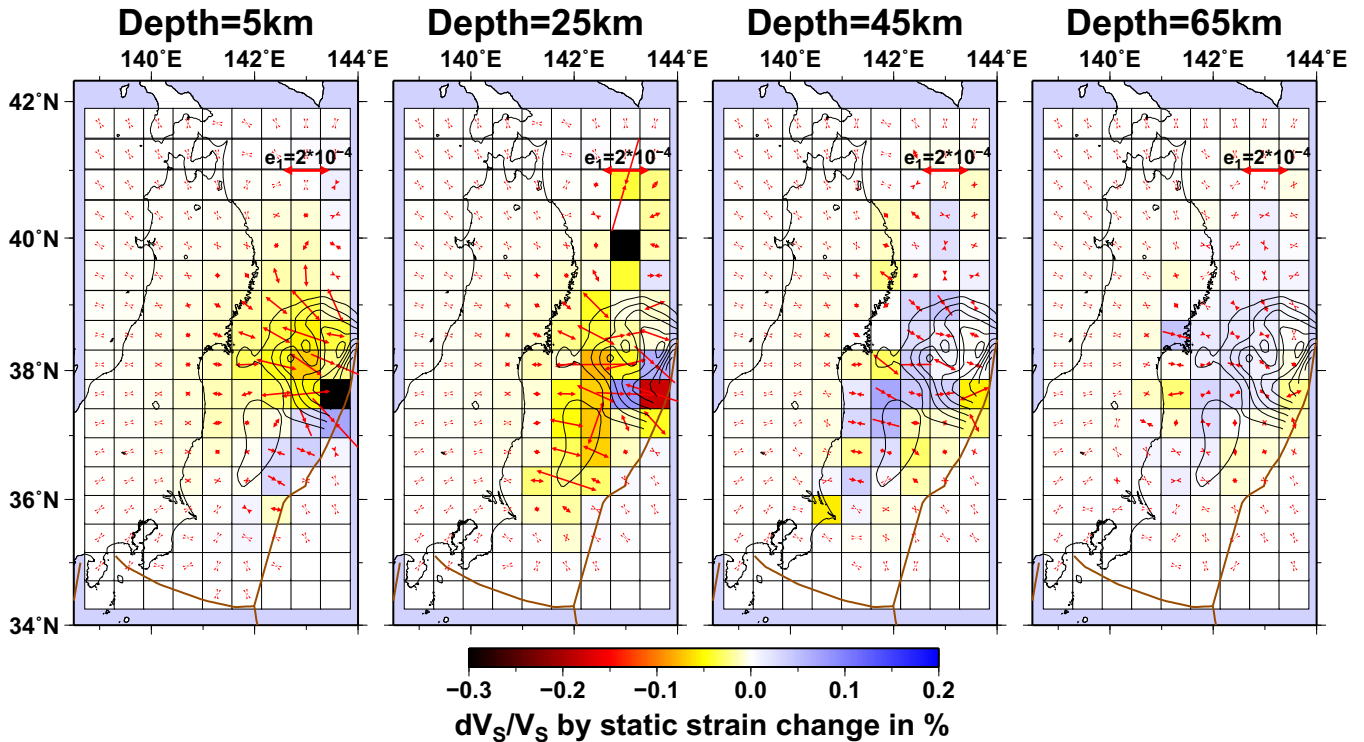


Figure 12. Map of V_S change ratio at depths of 5, 25, 45 and 65 km calculated from the observed static strain change and the finite deformation theory. The direction and value of the maximum principal strain change is shown by red arrows unless the amount of strain change exceeds 5×10^{-4} . The colour scale of the V_S change ratio is shown on the bottom of the figure. The black contour curves represent slip distribution of the Tohoku earthquake by 10 m slip interval following Iinuma *et al.* (2012).

calculated principal strain changes are converted to velocity change ratios using eq. (13). Here we use $C_{111} = -3100$ GPa, $C_{112} = -800$ GPa, and $C_{123} = 40$ GPa following the rock experiment by Prioul *et al.* (2004) that performed under hydrostatic stress of 30–100 MPa which corresponds to 1–4 km depth in the crust. $C_{11}^0 = 135$ GPa and $C_{44}^0 = 45$ GPa are also used as typical values in the lithosphere. The calculated S -wave velocity change ratio is mapped into Fig. 12 by coloured rectangles. Even though the obtained velocity change is anisotropic, we map average of the velocity changes for three directions calculated from eq. (13).

The maximum principal strain change mostly appears as dilations approximately along the east-west direction with values larger than 10^{-4} near the large slip area at depths of 5 and 25 km. At depths of 45 and 65 km, on the other hand, compaction along the east-west direction becomes dominant because these depths are below the plate boundary near the large slip area. A double-couple source produces a quadratic pattern of compressed and dilated zones. Consequently, V_S generally decreases at depths of 5 and 25 km and increases at depths of 45 and 65 km. The amount of evaluated V_S change ratio is mostly lower than 0.1 per cent except for some rectangles close to the faulting zone. Although not shown in the figure, the V_P change ratio is almost the same value to the V_S change ratio. This result is consistent with the conclusion of chapter 5; the velocity reductions at zones 3 and 4 are much smaller than 0.1 per cent.

Note that the TOE constants used in this section are measured under a hydrostatic stress corresponds to 1–4 km depths. The TOE constants at the depths greater than 4 km should be smaller than the measured values (see fig. 1 of Prioul *et al.* 2004). Therefore, the amount of evaluated velocity changes at 25, 45 and 65 km in Fig. 12 should be overestimated.

6.2 Velocity change along the faulting zone

We found that the sensitivity of phase delay curve to the velocity change along the faulting zone is very weak. Therefore, it is difficult to constrain the velocity change at this zone from the data used in this study. According to the core-sampling observation by Chester *et al.* (2013), the thickness of the fracturing zone is less than 5 m for the large slip area of the Tohoku earthquake, which is much narrower than the adapted thickness of 150 m in our numerical simulation. The phase delays due to the velocity reductions in such narrow zone would be even smaller than the results shown in Fig. 10.

However, there are some studies that directly detected velocity changes along the faulting zone. Chen *et al.* (2008) found a phase change for the direct S -wave of repeating earthquake seismograms after the 1999 Chi-Chi earthquake, Taiwan (M_w 7.6), and attributed this change to damage along faulting zone of the Chi-Chi earthquake. Yang *et al.* (2014) numerically demonstrated that the velocity change along the Jiangyou-Guanxian fault in China can explain the observed change in waveforms excited by the active source of ACROSS (Yamaoka *et al.* 2001). For the Tohoku earthquake, also, velocity reduction in the fractured zone along the plate boundary would exist. If seismograms recorded near the faulting zone that reaches to the ground surface (situation for the Chi-Chi earthquake) is available, the observed phase delay curve should be much more sensitive to the damage in the faulting zone and we would be able to detect the velocity change at there. However, this is not the case for the Tohoku earthquake and used Hi-net stations.

To monitor the damaging and recovery process of the faulting zone is of great importance in terms of understanding earthquake cycle and aftershock activity. If waves trapped by the fractured

zone are available (e.g. Peng & Ben-Zion 2004), velocity changes at such zone would be observable. For deep in-slab earthquakes, high-frequency waves are guided by the subducting oceanic slab (Furumura & Kennet 2005) and such waves may effectively detect velocity change along the faulting zone. However, the detail of short-wavelength structure of the subducting slab is still not well understood. Sensitivity of phase delay curve to the along-fault velocity change should be examined in a future study, which requires data obtained closer to the faulting zone and a massively parallel computing.

6.3 Time-lapse recovery of velocity

To interpret the time-lapse recovery process at deep zone, post-seismic deformation must be considered well. From Figs 4(a) and 6, we see a small recovery in the apparent velocity continuing more than 1 yr, while the V_S at the shallow subsurface recovers more quickly. This result indicates that relative contribution of velocity change at deep zone gradually becomes important at long lapse time as the velocity of shallow subsurface recovers. Because a large scale post-seismic deformation continues over 1 yr after the Tohoku earthquake, especially at the deep zone along the plate boundary (e.g. Ozawa *et al.* 2012), the velocity change at the deep zone may accompany with this deformation. Both afterslip and viscoelastic relaxation are candidate of the post-seismic deformation. These two phenomena affect the static strain change differently; the former redistributes the static strain in the lithosphere, while the latter relieves the static strain and recovers it to the pre-main shock condition. In addition, induced seismicity after the main shock brings secondary damage, which also reduces the velocity of the medium. The combination of these phenomena may ultimately result in the slow recovery at the deep zone. It is interesting to apply the finite deformation theory used in Section 6.1 to post-seismic deformation observed in different periods after the main shock, and evaluate how the distribution of velocity change varies with time.

7 CONCLUSION

Applying the MTWCA to seismograms of repeating earthquakes occurring before and after the 2011 Tohoku earthquake, Japan, we measure phase delay curves for cluster–station pairs distributed in northeastern Japan. The apparent velocity change ratio (negative of slope of the phase delay curve) shows a spatial variation; offshore region shows larger apparent velocity reductions. The apparent velocity reductions detected for the *S*-wave time window are up to 0.2 per cent, while that for the *P*-wave time window are up to 0.1 per cent. To examine the sensitivity of the observed phase delay curve to the partial velocity change, we perform a 2-D FD wave propagation simulation employing a realistic velocity model. From a forward modelling, we confirm that the observed phase delay curves are explained well by a 1 per cent velocity reduction at 0–150 m depth. The evaluated velocity reduction ratio is consistent with the previous study on velocity reduction detected at the shallow subsurface which is exposed to strong ground motion of the main shock. In the deeper zone, down to 80 km depth, the velocity reduction ratio is evaluated to be much smaller than 0.1 per cent. Applying the finite deformation theory to static strain change by the Tohoku earthquake and its post-seismic deformation, we found that the static strain change well explains the evaluated small velocity change. The recovery speed of velocity in the deep zone is slower than that near the ground surface. Displacement of location of the

repeating cluster after the Tohoku earthquake is not likely the primary cause of the observed phase delay according to the numerical simulation.

ACKNOWLEDGEMENTS

The Hi-net records are available through the webpage of NIED (<http://www.hinet.bosai.go.jp/?LANG=en>). We are grateful to Dr T. Iinuma for providing us with the slip distribution model, and thank Dr K.H. Chen for useful comments and suggestions. We also thank Dr J. Trampert, editor-in-Chief of Geophysical Journal International, and two anonymous reviewers for thoughtful comments to improve our manuscript. This study is partly supported by Japan Society for the Promotion of Science (JSPS grants 22.1224). Seismic Analysis Code (SAC) and Generic Mapping Tools (GMT) are used for signal processing and figure plotting, respectively.

REFERENCES

- Aster, R.C., Borchers, B. & Thurber, C.H., 2011. *Parameter Estimation and Inverse Problems*, Elsevier, 260 pp.
- Brenguier, F., Campillo, M., Hadziioannou, C., Shapiro, N.M., Nadeau, R.M. & Larose, E., 2008. Postseismic relaxation along the San Andreas Fault at Parkfield from continuous seismological observations, *Science*, **321**, 1478–1481.
- Brenguier, F., Campillo, M., Takeda, T., Aoki, Y., Shapiro, N.M., Briand, X., Emoto, K. & Miyake, H., 2014. Mapping pressurized volcanic fluids from induced crustal seismic velocity drops, *Science*, **345**, 80–82.
- Chen, K.H., Nadeau, R.M. & Rau, R.J., 2008. Characteristic repeating earthquakes in an arc-continent collision boundary zone: the Chihshang fault of eastern Taiwan, *Earth planet. Sci. Lett.*, **276**(3–4), 262–272.
- Chester, F.M. *et al.*, 2013. Structure and composition of the plate-boundary slip zone for the 2011 Tohoku-Oki earthquake, *Science*, **342**, 1208–1211.
- Fujiwara, T., Kodaira, S., No, T., Kaiho, Y., Takahashi, N. & Kaneda, Y., 2011. The 2011 Tohoku-Oki earthquake: displacement reaching the trench axis, *Science*, **334**, 1240–1240.
- Furumura, T. & Kennet, B.L.N., 2005. Subduction zone guided waves and the heterogeneity structure of the subducted plate: intensity anomalies in northern Japan, *J. geophys. Res.*, **110**, B10302, doi:10.1029/2004JB003486.
- Furumura, T., Takemura, S., Noguchi, S., Takemoto, T., Maeda, T., Iwai, K. & Padhy, S., 2011. Strong ground motions from the 2011 off-the Pacific Coast-of-Tohoku, Japan (Mw = 9.0) earthquake obtained from a dense nationwide seismic network, *Landslides*, **8**, 333–338.
- Gardner, G.H.F., Gardner, L.W. & Gregory, A.R., 1974. Formation velocity and density - the diagnostic basics for stratigraphic traps, *Geophysics*, **39**, 770–780.
- Hearmon, R.F.S., 1953. Third-order elastic coefficients, *Acta Crystallogr.*, **6**, 331–340.
- Hobiger, M., Wegler, U., Shiomi, K. & Nakahara, H., 2012. Coseismic and postseismic elastic wave velocity variations caused by the 2008 Iwate-Miyagi Nairiku earthquake, Japan, *J. geophys. Res.*, **117**, B09313, doi:10.1029/2012JB009402.
- Iinuma, T. *et al.*, 2012. Coseismic slip distribution of the 2011 off the Pacific Coast of Tohoku Earthquake (M9.0) refined by means of seafloor geodetic data, *J. geophys. Res.*, **117**, B07409, doi:10.1029/2012JB009186.
- Ito, A., 1990. Earthquake swarm activity revealed from high-resolution relative hypocenters – clustering of microearthquakes, *Tectonophysics*, **175**(1), 47–66.
- Kido, M., Osada, Y., Fujimoto, H., Hino, R. & Ito, Y., 2011. Trench-normal variation in observed seafloor displacements associated with the 2011 Tohoku-Oki earthquake, *Geophys. Res. Lett.*, **38**, L24303, doi:10.1029/2011GL050057.
- Kodaira, S. *et al.*, 2012. Coseismic fault rupture at the trench axis during the 2011 Tohoku-oki earthquake, *Nat. Geosci.*, **5**, 646–650.

- Maeda, T., Obara, K. & Yukutake, Y., 2010. Seismic velocity decrease and recovery related to earthquake swarms in a geothermal area, *Earth Planets Space*, **62**, 685–691.
- Maeda, T., Obara, K., Furumura, T. & Saito, T., 2011. Interference of long-period seismic wavefield observed by the dense Hi-net array in Japan, *J. geophys. Res.*, **116**, B10303, doi:10.1029/2011JB008464.
- Margerin, L., Campillo, M. & van-Tiggelen, B., 2000. Monte Carlo simulation of multiple scattering of elastic waves, *J. geophys. Res.*, **105**(B4), 7873–7892.
- Minato, S., Tsuji, T., Ohmi, S. & Matsuoka, T., 2012. Monitoring seismic velocity change caused by the 2011 Tohoku-oki earthquake using ambient noise records, *Geophys. Res. Lett.*, **39**, L03909, doi:10.1029/2012GL051405.
- Murnaghan, F.D., 1967. *Finite Deformation of an Elastic Solid*, Dover, 124 pp.
- Nakajima, J., Matsuzawa, T., Hasegawa, A. & Zhao, D., 2001. Three-dimensional structure of V_p , V_s , and V_p/V_s beneath northeastern Japan: implications for arc magmatism and fluids, *J. geophys. Res.*, **106**(B10), 21 843–21 857.
- Nishimura, T. *et al.*, 2005. Temporal changes in seismic velocity of the crust around Iwate volcano, Japan, as inferred from analyses of repeated active seismic experiment data from 1998 to 2003, *Earth Planets Space*, **57**, 491–505.
- Obara, K., Kasahara, K., Hori, S. & Okada, Y., 2005. A densely distributed high-sensitivity seismograph network in Japan: Hi-net by National Research Institute for Earth Science and Disaster Prevention, *Rev. Scient. Instrum.*, **76**, 021301, doi:10.1063/1.1854197.
- Obermann, A., Planès, T., Larose, E., Sens-Schönfelder, C. & Campillo, M., 2013. Depth sensitivity of seismic coda waves to velocity perturbations in an elastic heterogeneous medium, *Geophys. J. Int.*, **194**(1), 372–382.
- Okada, Y., 1992. Internal deformation due to shear and tensile faults in a half-space, *Bull. seism. Soc. Am.*, **82**(2), 1018–1040.
- Ozawa, S., Nishimura, T., Munekane, H., Suito, H., Kobayashi, T., Tobita, M. & Imakiire, T., 2012. Preceding, coseismic, and postseismic slips of the 2011 Tohoku earthquake, Japan, *J. geophys. Res.*, **117**, B07404, doi:10.1029/2011JB009120.
- Peng, Z. & Ben-Zion, Y., 2004. Systematic analysis of crustal anisotropy along the Karadere-Düzce branch of the North Anatolian fault, *Geophys. J. Int.*, **159**(1), 253–274.
- Peng, Z. & Ben-Zion, Y., 2006. Temporal changes of shallow seismic velocity around the Karadere-Duzce branch of the North Anatolian fault and strong ground motion, *Pure appl. Geophys.*, **163**, 567–600.
- Poupinet, G., Ellsworth, W.L. & Frechet, J., 1984. Monitoring velocity variations in the crust using earthquake doublets: an application to the Calaveras fault, California, *J. geophys. Res.*, **89**, 5719–5731.
- Prioul, R., Bakulin, A. & Bakulin, V., 2004. Nonlinear rock physics model for estimation of 3D subsurface stress in anisotropic formations: theory and laboratory verification, *Geophysics*, **69**(2), 415–425.
- Rivet, D., Campillo, M., Shapiro, N.M., Cruz-Atienza, V., Radiguet, M., Cotte, N. & Kostoglodov, V., 2011. Seismic evidence of nonlinear crustal deformation during a large slow slip event in Mexico, *Geophys. Res. Lett.*, **38**, L08308, doi:10.1029/2011GL047151.
- Rubinstein, J.L. & Beroza, G.C., 2005. Depth constraints on nonlinear strong ground motion from the 2004 Parkfield earthquake, *Geophys. Res. Lett.*, **32**, L14313, doi:10.1029/2005GL023189.
- Rubinstein, J.L., Uchida, N. & Beroza, G.C., 2007. Seismic velocity reductions caused by the 2003 Tokachi-Oki earthquake, *J. geophys. Res.*, **112**, B05315, doi:10.1029/2006JB004440.
- Sánchez-Sesma, F.J. & Campillo, M., 2006. Retrieval of the Green's function from cross correlation: the canonical elastic problem, *Bull. seism. Soc. Am.*, **96**(3), 1182–1191.
- Satake, K., Fujii, Y., Harada, T. & Namegaya, Y., 2013. Time and space distribution of coseismic slip of the 2011 Tohoku earthquake as inferred from tsunami waveform data, *Bull. seism. Soc. Am.*, **103**, 1473–1492.
- Sato, H., 2008. Synthesis of vector-wave envelopes in 3-D random media characterized by a nonisotropic Gaussian ACF based on the Markov approximation, *J. geophys. Res.*, **113**, B08304, doi:10.1029/2007JB005524.
- Sato, H., Fehler, M.C. & Maeda, T., 2012. *Seismic Wave Propagation and Scattering in the Heterogeneous Earth*, Springer-Verlag.
- Sato, M., Ishikawa, T., Ujihara, N., Yoshida, S., Fujita, M., Mochizuki, M. & Asada, A., 2011. Displacement above the hypocenter of the 2011 Tohoku-Oki earthquake, *Science*, **332**, 1395, doi:10.1126/science.1207401.
- Sawazaki, K. & Snieder, R., 2013. Time-lapse changes of P - and S -wave velocities and shear wave splitting in the first year after the 2011 Tohoku earthquake, Japan: shallow subsurface, *Geophys. J. Int.*, **193**(1), 238–251.
- Shiomi, K., Obara, K., Aoi, S. & Kasahara, K., 2003. Estimation on the azimuth of the Hi-net and KiK-net borehole seismometers (in Japanese), *Zisin*, **56**, 99–110.
- Snieder, R. & Vrijlandt, M., 2005. Constraining the source separation with coda wave interferometry: theory and application to earthquake doublets in the Hayward fault, California, *J. geophys. Res.*, **110**(B4), B04301, doi:10.1029/2004JB003317.
- Snieder, R., Grêt, A., Douma, H. & Scales, J., 2002. Coda wave interferometry for estimating nonlinear behavior in seismic velocity, *Science*, **295**, 2253–2255.
- Suzuki, W., Aoi, S., Sekiguchi, H. & Kunugi, T., 2011. Rupture process of the 2011 Tohoku-Oki mega-thrust earthquake (M9.0) inverted from strong-motion data, *Geophys. Res. Lett.*, **38**, L00G16, doi:10.1029/2011GL049136.
- Takagi, R. & Okada, T., 2012. Temporal change in shear velocity and polarization anisotropy related to the 2011 M9.0 Tohoku-Oki earthquake examined using KiK-net vertical array data, *Geophys. Res. Lett.*, **39**, L09310, doi:10.1029/2012GL051342.
- Takagi, R., Okada, T., Nakahara, H., Umino, N. & Hasegawa, A., 2012. Coseismic velocity change in and around the focal region of the 2008 Iwate-Miyagi Nairiku earthquake, *J. geophys. Res.*, **117**, B06315, doi:10.1029/2012GL051342.
- Tsvankin, I., 2001. *Seismic Signatures and Analysis of Reflection Data in Anisotropic Media*, Pergamon.
- Uchida, N. & Matsuzawa, T., 2013. Pre- and postseismic slow slip surrounding the 2011 Tohoku-oki earthquake rupture, *Earth planet. Sci. Lett.*, **374**, 81–91.
- Uchida, N., Shimamura, K., Matsuzawa, T. & Okada, T., 2015. Postseismic response of repeating earthquakes around the 2011 Tohoku-oki earthquake: moment increases due to the fast loading rate, *J. geophys. Res.*, **120**(1), 259–274.
- Weaver, R.L., 1982. On diffuse waves in solid media, *J. acoust. Soc. Am.*, **71**, 1608, doi:10.1121/1.387816.
- Wegler, U. & Sens-Schönfelder, C., 2007. Fault zone monitoring with passive image interferometry, *Geophys. J. Int.*, **168**(3), 1029–1033.
- Wegler, U., Nakahara, H., Sens-Schönfelder, C., Korn, M. & Shiomi, K., 2009. Sudden drop of seismic velocity after the 2004 Mw 6.6 mid-Niigata earthquake, Japan, observed with Passive Image Interferometry, *J. geophys. Res.*, **114**, B06305, doi:10.1029/2008JB005869.
- Yamaoka, K., Kunitomo, T., Miyakawa, K., Kobayashi, K. & Kumazawa, M., 2001. A trial for monitoring temporal variation of seismic velocity using an ACROSS system, *Island Arc*, **10**(3–4), 336–347.
- Yang, W., Ge, H., Wang, B., Hu, J., Yuan, S. & Qiao, S., 2014. Active source monitoring at the Wenchuan fault zone: coseismic velocity change associated with aftershock event and its implication, *Earthq. Sci.*, **27**(6), 599–606.
- Yoshida, Y., Ueno, H., Muto, D. & Aoki, S., 2011. Source process of the 2011 off the Pacific coast of Tohoku earthquake with the combination of teleseismic and strong motion data, *Earth Planets Space*, **63**, 565–569.
- Yu, W.C., Song, T.R.A. & Silver, P.G., 2013. Temporal velocity changes in the crust associated with the Great Sumatra earthquakes, *Bull. seism. Soc. Am.*, **103**(5), 2797–2809.

APPENDIX A: POWER OF THE HANNING WINDOW FUNCTION

The Hanning window function H is given in the frequency domain by

$$\begin{aligned} H(f) &= 0.5/\Delta f & (f = 0) \\ &= 0.25/\Delta f & (f = \pm\Delta f) \\ &= 0 & (|f| > \Delta f), \end{aligned} \tag{A1}$$

where Δf is the sampling interval in the frequency domain given by $\Delta f = 1/T$. The power of the Hanning window I is thus given by

$$I = \int_{-\infty}^{\infty} H(f)^2 df = (0.5^2 + 2 \cdot 0.25^2)/\Delta f^2 \cdot \Delta f = 0.375T. \tag{A2}$$

APPENDIX B: VELOCITY CHANGE RATIO DERIVED FROM THE FINITE DEFORMATION THEORY

According to Hearmon (1953), the isotropic TOE tensor is given by

$$\begin{aligned} C_{1\beta\gamma}^1 &= \begin{pmatrix} C_{111} & C_{112} & C_{112} & 0 & 0 & 0 \\ C_{112} & C_{112} & C_{123} & 0 & 0 & 0 \\ C_{112} & C_{123} & C_{112} & 0 & 0 & 0 \\ 0 & 0 & 0 & C_{144} & 0 & 0 \\ 0 & 0 & 0 & 0 & C_{155} & 0 \\ 0 & 0 & 0 & 0 & 0 & C_{155} \end{pmatrix}, & C_{2\beta\gamma}^1 &= \begin{pmatrix} C_{112} & C_{112} & C_{123} & 0 & 0 & 0 \\ C_{112} & C_{111} & C_{112} & 0 & 0 & 0 \\ C_{123} & C_{112} & C_{112} & 0 & 0 & 0 \\ 0 & 0 & 0 & C_{155} & 0 & 0 \\ 0 & 0 & 0 & 0 & C_{144} & 0 \\ 0 & 0 & 0 & 0 & 0 & C_{155} \end{pmatrix}, \\ C_{3\beta\gamma}^1 &= \begin{pmatrix} C_{112} & C_{123} & C_{112} & 0 & 0 & 0 \\ C_{123} & C_{112} & C_{112} & 0 & 0 & 0 \\ C_{112} & C_{112} & C_{111} & 0 & 0 & 0 \\ 0 & 0 & 0 & C_{155} & 0 & 0 \\ 0 & 0 & 0 & 0 & C_{155} & 0 \\ 0 & 0 & 0 & 0 & 0 & C_{144} \end{pmatrix}, & C_{4\beta\gamma}^1 &= \begin{pmatrix} 0 & 0 & 0 & C_{144} & 0 & 0 \\ 0 & 0 & 0 & C_{155} & 0 & 0 \\ 0 & 0 & 0 & C_{155} & 0 & 0 \\ C_{144} & C_{155} & C_{155} & 0 & 0 & 0 \\ 0 & 0 & 0 & 0 & 0 & C_{456} \\ 0 & 0 & 0 & 0 & C_{456} & 0 \end{pmatrix}, \\ C_{5\beta\gamma}^1 &= \begin{pmatrix} 0 & 0 & 0 & 0 & C_{155} & 0 \\ 0 & 0 & 0 & 0 & C_{144} & 0 \\ 0 & 0 & 0 & 0 & C_{155} & 0 \\ 0 & 0 & 0 & 0 & 0 & C_{456} \\ C_{155} & C_{144} & C_{155} & 0 & 0 & 0 \\ 0 & 0 & 0 & C_{456} & 0 & 0 \end{pmatrix}, & C_{6\beta\gamma}^1 &= \begin{pmatrix} 0 & 0 & 0 & 0 & 0 & C_{155} \\ 0 & 0 & 0 & 0 & 0 & C_{155} \\ 0 & 0 & 0 & 0 & 0 & C_{144} \\ 0 & 0 & 0 & 0 & C_{456} & 0 \\ 0 & 0 & 0 & C_{456} & 0 & 0 \\ C_{155} & C_{155} & C_{144} & 0 & 0 & 0 \end{pmatrix}, \end{aligned} \tag{B1}$$

where

$$\begin{aligned} C_{144} &= \frac{1}{2}(C_{112} - C_{123}) \\ C_{155} &= \frac{1}{4}(C_{111} - C_{112}) \\ C_{456} &= \frac{1}{8}C_{111} - \frac{3}{8}C_{112} + \frac{1}{4}C_{123}. \end{aligned} \tag{B2}$$

Taking the Cartesian coordinate system along the principal strains, we obtain

$$\Delta\varepsilon_1 = \varepsilon_1, \quad \Delta\varepsilon_2 = \varepsilon_2, \quad \Delta\varepsilon_3 = \varepsilon_3, \quad \Delta\varepsilon_4 = \Delta\varepsilon_5 = \Delta\varepsilon_6 = 0. \tag{B3}$$

Using eqs (B1), (B2), (B3) and (12), we obtain

$$\begin{aligned}
 \Delta C_{11} &= C_{111}\varepsilon_1 + C_{112}(\varepsilon_2 + \varepsilon_3) \\
 \Delta C_{22} &= C_{111}\varepsilon_2 + C_{112}(\varepsilon_1 + \varepsilon_3) \\
 \Delta C_{33} &= C_{111}\varepsilon_3 + C_{112}(\varepsilon_1 + \varepsilon_2) \\
 \Delta C_{12} &= \Delta C_{21} = C_{123}\varepsilon_3 + C_{112}(\varepsilon_1 + \varepsilon_2) \\
 \Delta C_{23} &= \Delta C_{32} = C_{123}\varepsilon_1 + C_{112}(\varepsilon_2 + \varepsilon_3) \\
 \Delta C_{13} &= \Delta C_{31} = C_{123}\varepsilon_2 + C_{112}(\varepsilon_1 + \varepsilon_3) \\
 \Delta C_{44} &= C_{144}\varepsilon_1 + C_{155}(\varepsilon_2 + \varepsilon_3) \\
 \Delta C_{55} &= C_{144}\varepsilon_2 + C_{155}(\varepsilon_1 + \varepsilon_3) \\
 \Delta C_{66} &= C_{144}\varepsilon_3 + C_{155}(\varepsilon_1 + \varepsilon_2) \\
 \text{other components} &= 0.
 \end{aligned}
 \tag{B4}$$

Therefore, applying arbitrary strain to an isotropic medium produces an orthorhombic anisotropic medium with nine independent constants (Tsvankin 2001). For this anisotropic medium under the applied strain, we denote *P*-wave velocity propagates along *i* direction (*i* = 1, 2, 3) as V_{Pi} , and *S*-wave velocity propagates along *i* direction polarizing along *j* direction (*i* ≠ *j*) as V_{Sij} . They are described as

$$\begin{aligned}
 V_{Pi} &= \sqrt{\frac{C_{ii}^0 + \Delta C_{ii}}{\rho_0 + \Delta\rho}} \\
 V_{Sij} = V_{Sji} &= \sqrt{\frac{C_{(k+3)(k+3)}^0 + \Delta C_{(k+3)(k+3)}}{\rho_0 + \Delta\rho}} \quad (k \neq i, k \neq j) \\
 \Delta\rho &= -\rho_0 \sum_{i=1}^3 \varepsilon_i,
 \end{aligned}
 \tag{B5}$$

where $\Delta\rho$ is change of mass density by the volumetric strain change.

The velocity change ratios are thus derived as

$$\begin{aligned}
 \frac{\Delta V_{Pi}}{V_{Pi}^0} &= \frac{V_{Pi} - V_{Pi}^0}{V_{Pi}^0} \approx \frac{\Delta C_{ii}}{2C_{ii}^0} - \frac{\Delta\rho}{2\rho_0} \\
 &= \frac{1}{2C_{11}^0} [C_{111}\varepsilon_i + C_{112}(\varepsilon_j + \varepsilon_k)] + \frac{1}{2} \sum_{l=1}^3 \varepsilon_l \\
 \frac{\Delta V_{Sij}}{V_{Sij}^0} &= \frac{\Delta V_{Sji}}{V_{Sji}^0} = \frac{V_{Sij} - V_{Sij}^0}{V_{Sij}^0} \approx \frac{\Delta C_{(k+3)(k+3)}}{2C_{(k+3)(k+3)}^0} - \frac{\Delta\rho}{2\rho_0} \\
 &= \frac{1}{2C_{44}^0} [C_{144}\varepsilon_k + C_{155}(\varepsilon_i + \varepsilon_j)] + \frac{1}{2} \sum_{l=1}^3 \varepsilon_l.
 \end{aligned}
 \tag{B6}$$